Insights into Energetic Penalties in Electrochemical CO_2 Separation Systems

*Lauren E. Clarke and Fikile R. Brushett**

Department of Chemical Engineering, Massachusetts Institute of Technology, Cambridge, Massachusetts 02139, United States

* Corresponding author (F.R. Brushett, brushett@mit.edu)

ABSTRACT

While innovative electrochemical approaches continue to emerge for carbon capture, open questions remain regarding the performance characteristics of these nascent concepts. A wide range of energy requirements have been reported; the different sources of performance loss and their relative magnitudes are not yet fully understood, challenging both quantitative comparisons between devices and identification of performance improvement pathways. Herein, we develop a mathematical framework to evaluate the energetics of four-stage electrochemical separation systems in which soluble capture chemistries are activated and deactivated in an electrochemical reactor, and bind and release carbon dioxide (CO_2) in separate units. Specifically, we construct a dimensionless electrochemical reactor model, derive key groups associated with thermodynamics, kinetics, ohmic resistance, and mass transport, and, subsequently, evaluate their impact on energetic penalties. We also discuss the use of this model for exploring different performance improvement pathways. Ultimately, this work seeks to facilitate understanding of the interplay between material properties, operating conditions, and energy requirements.

Keywords: Electrochemical carbon dioxide capture, electrochemical reactor modeling, energy loss breakdown, electrochemical engineering

1. INTRODUCTION

Limiting global temperature rise will require a panoply of low-carbon, net-zero, and net-negative technologies.[1] Carbon capture and utilization or storage (CCUS) represent a promising class of systems that are expected to aid in this transition by mitigating emissions of existing infrastructure, addressing hard-to-decarbonize sources, and enabling net-negative processes.[1,2] The deployment of CCUS has grown in the past few years; at the time of writing, there are >500 CCUS projects (at various scales) in different development stages, ~40 of which are operational and have the collective capacity to remove >45 million metric tons of carbon dioxide (CO_2) each year,[3] or ~0.1% of 2022 global CO_2 emissions.[4] Despite this growth, the projected carbon capture capacity in 2030 is only a third of the 1.2 Gt CO_2 yr^{-1} called for in the Net Zero Emissions by 2050 Scenario.[5] This will need to scale further by 2050, when the expected requirement for carbon capture capacity increases to 6.2 Gt CO_2 yr^{-1}.[5] A major limitation to achieving this scale is the cost of these technologies. When considering carbon capture and storage (i.e., CCS), the capture/separation step comprises ~70–90% of process costs due to the dilute CO_2 concentration (and thus higher flow rates of gases that are handled per unit quantity of CO_2 separated), the high energy requirements of the capture process, and the presence of impurities that may need to be removed prior to CO_2 separation.[6] Accordingly, efforts have been dedicated to address these challenges and in so doing reduce CO_2 separation costs. Common approaches to carbon capture involve absorption or adsorption, whereby CO_2 is absorbed (or adsorbed) by a liquid solvent (or solid sorbent), which is an enthalpy-driven, spontaneous process at ambient temperatures. Then, the temperature is increased to overcome the positive enthalpy change and drive the release of CO_2, while also regenerating the solvent (or sorbent).[7–10] Of these types of processes, chemical absorption with amine-based solvents is currently the most mature and widely deployed carbon capture method.[7]

However, the high system energy requirements associated with the desorption step are a limiting factor, leading to high energy costs. In addition, these processes typically rely on fossil-fuel derived heat to drive separation, limiting their effectiveness for mitigating CO_2 emissions.[6]

Electrochemical CO_2 separation is an emerging approach for carbon capture, where differences in electrical potential, rather than temperature, serve as a driving force.[11] Specifically, the electrode potential is modulated to drive redox reactions that activate or deactivate the capture media, driving CO_2 capture or release, respectively. Utilizing electrochemical technologies offers several advantages, such as the ability to achieve higher energetic efficiencies and to be directly coupled with renewable electricity sources, improving their ability for CO_2 abatement. Other beneficial characteristics include modular design (enabling both scale up and down), as well as the ability to operate at (or near) ambient conditions. Research on electrochemical CO_2 separation has developed over the past 10–20 years due, at least in part, to a growing recognition of the urgency of climate change. During this time, several different approaches for electrochemically-driven carbon capture have been introduced, which can broadly be classified as either direct or indirect processes.[12] In direct methods, the capture molecule is redox-active, and its CO_2 binding affinity is directly altered via electrode reactions. For indirect systems, the capture molecule itself is not redox-active; instead, a redox-active competitor molecule can be electrochemically reduced/oxidized to change its affinity for the capture molecule, thus impacting the ability for the capture molecule to bind/release CO_2. A variety of these chemistry concepts have been experimentally studied in different laboratory set-ups, ranging from small-scale cells (e.g., 3-electrode cells for electroanalytical studies, H-cells for bulk electrolysis) to bench-scale systems implementing flow-cells and auxiliary units (e.g., absorber).[13] Such innovative, yet early-stage, demonstrations evince the feasibility of electrochemical CO_2 separation and hint at its potential as

compared to current carbon capture methods. Specifically, recent work has estimated that CO_2 can be separated in lab-scale prototypes with cell energy requirements of 35–430 kJ (mol CO_2)$^{-1}$ (for separation from ~15 mol% CO_2 mixtures).[14–19] These findings suggest that certain electrochemical processes may be competitive with state-of-the-art amine absorption processes used for post-combustion capture, which typically require ca. 100–180 kJ (mol CO_2)$^{-1}$ of heat for the desorption step.[20–22,22–25] Despite this promise, several open questions remain regarding the performance of electrochemical CO_2 separation systems and how these conceptual processes may be effectively translated to engineered systems at scale. First, when considering the range of energy requirements reported, it is unclear what resistive losses contribute most significantly to the total energy needs, what pathways exist for reducing those losses through materials innovation, reactor engineering, and/or process design, and what tradeoffs must be managed to enable operation in energetically-efficient regimes. Given the nascency of these separation approaches, engineering analyses, enabled by mathematical modeling, may serve as a useful guide, as has been the case for other emerging electrochemical technologies.[26–30] Overall, cell and/or system modeling can aid in understanding performance characteristics of new concepts, identifying appropriate materials properties, scales, and conditions for efficient and economic operation, and facilitating quantitative comparisons with other current or emerging methods.

For all modeling analyses, the minimum work of separation serves as a lower bound on energy requirements and can be determined from the Gibbs free energy difference between the inlet (CO_2-rich feed gas) and outlet (high-purity CO_2 product and CO_2-lean raffinate) streams. For a hypothetical case of "skimming", where an infinitesimal quantity of CO_2 is removed from a feed gas, the minimum work can be represented as:[9]

$$W_{\min} = -R_u T \ln\left(\frac{P_{CO_2,feed}}{P_0}\right) \quad (1)$$

Here, W_{min} is the minimum work (J (mol CO_2)$^{-1}$), R_{u} is the ideal gas constant (8.314 J mol^{-1} K^{-1}), T is the absolute temperature (K), $P_{\mathrm{CO_2,feed}}$ is the partial pressure of CO_2 in the feed gas (Pa), and P_0 is the ambient pressure (101325 Pa). In this equation, it is assumed that all gases (i.e., CO_2-rich feed gas, CO_2-depleted raffinate, and recovered CO_2 product) are at temperature, T, and ambient pressure, P_0. Considering a separation case where CO_2 is captured from a 15 mol% feedstock, which is representative of flue gas compositions in post-combustion capture for coal-fired power plants,[31] the minimum work in the limit of "skimming" is 4.7 kJ (mol CO_2)$^{-1}$. For a more practical scenario, where a certain fraction of the CO_2 is removed from the feed gas, the minimum work can be determined using equations detailed in prior works.[9,32] For 90% CO_2 removal from a 15% feedstock, a common limit in post-combustion capture processes,[8,33] the minimum work increases to 6.4 kJ (mol CO_2)$^{-1}$.

Thermodynamic analyses have been the focus of prior modeling efforts to understand upper performance bounds of electrochemical separation processes (beyond W_{min}) and to investigate how different system/molecular properties impact these limits.[32,34,35] In brief, four system configurations have been proposed and evaluated, each resulting in a different thermodynamic cycle for separation and, thus, distinct performance characteristics.[32,34,35] In a four-stage system, a capture molecule is activated, either directly or indirectly, in an electrochemical cell by cathodic reduction (stage 1). Following this step, the capture media is exposed to a CO_2-containing feed gas for absorption (stage 2). The capture media is then deactivated in an electrochemical cell by anodic oxidation (stage 3) which is followed by CO_2 release to a high-purity gas phase (stage 4). "Cathodic absorption" can be adopted to yield a three-stage system, where the capture media is exposed to the feed gas during the activation step, such that activation and binding occur simultaneously. Similarly, implementation of "anodic desorption" also results in a three-stage

system. In this configuration, the capture media is exposed to the product gas at the anode such that deactivation and release occur concurrently. The fourth configuration is referred to as a two-stage system, which consists of both cathodic absorption and anodic desorption. Previous analyses have shown that implementing cathodic absorption and/or anodic desorption can lower thermodynamic energy requirements by eliminating the differences between the CO_2 partial pressure following activation or deactivation and the CO_2 partial pressure in the feed gas or product gas.[32,34,36] This specifically results in chemical potential gradients between the ab-/adsorbed CO_2 and the external "reservoirs" of CO_2, leading to irreversible mass transfer.[37] If the capture media is considered as the system, and the external "reservoirs" of CO_2 are considered as the surroundings, these losses can be referred to as external irreversibilities. Therefore, although an ideal thermodynamic cycle for a four-stage system is internally reversible, where the cycle is characterized by moving through a series of equilibrium states, the predicted separation work deviates from the minimum work due to external irreversibilities. It has also been shown that the chemical potential gradients, and thus penalties due to external irreversibilities, can be reduced in a four-stage (or three-stage) system by tuning molecular/system properties,[32,34] but larger chemical potential gradients are also beneficial for operation at higher process rates (i.e., faster capture/release).[36,38]

While this earlier thermodynamic modeling has provided foundational understanding, there are additional sources of irreversibility that further diminish performance in operating systems. For example, fluid dynamic losses in the process units and connecting piping will occur and result in larger energy requirements from liquid pumps and gas compressors. Further, thermal management systems may be needed to control temperature during operation. However, it is anticipated that irreversible losses within the electrochemical reactor, beyond what is predicted in equilibrium

thermodynamic models, will play a significant role in system energetics and efficiency.[39] In general, there are several sources of irreversibility within an electrochemical device that increase the energy requirements beyond the thermodynamic limit. More specifically, operating a cell at elevated current densities, which is beneficial for process rates and reactor footprint, requires deviation from equilibrium (i.e., overpotentials) and thus, incurs energetic penalties. These overpotentials can occur due to a variety of sources, but are most commonly associated with reaction kinetics, electronic/ionic transport, and mass transport.[40] Electrochemical reactions require polarization of the electrode surface to overcome the activation barrier and drive the reaction at a particular rate. The electronic/ionic resistance to the flow of current within the cell, which is referred to as the ohmic resistance, is a function of the physical properties and geometries of the constituent components (e.g., electrodes, membranes/separators, flow fields, etc.). Finally, reactant/product concentration gradients that form within the cell result in mass transport resistances. Beyond these traditional sources of resistive loss, electrochemical CO_2 separation processes also involve solution-phase, homogeneous reactions (i.e., CO_2 binding/release), the kinetics of which influence required cell overpotentials. Researchers have started to evaluate how different sources of irreversibility within the cell contribute to the total separation work through modeling of different types of indirect capture chemistries;[36,39] however, more efforts are needed to identify the key molecular and cell properties that impact performance, to develop engineering guidelines for reducing energy requirements, and to highlight how current and emerging capture chemistries fit into this design space.

To this end, we develop a dimensionless cell model for electrochemical CO_2 separation systems to continue exploring energy requirements and irreversibilities, while specifically focusing on a four-stage system with a direct capture chemistry. We begin by explaining the modeling

framework and the dimensional equations required to determine species concentrations and electrode potentials. Then, we discuss the non-dimensionalization process, where we identify a reduced set of groups that govern overall performance. Finally, we describe how the separation work (i.e., energy requirements) is determined and discuss the computational approach/resources used to solve the outlined equations. Next, using this model, we revisit the thermodynamic cycle to set the lower limit on energy requirements for a four-stage system and quantify energetic penalties due to external irreversibilities. We independently probe and compare the relative magnitude of losses due to species electrochemical kinetics, homogeneous kinetics, ohmic resistance, and mass transport. Within each section, we discuss the key dimensionless variables associated with each phenomenon and explore how changing these parameters impact the energetics while also highlighting how coupling effects between different variables alter overall energy requirements. We use existing data from electrochemical CO_2 separation systems, as well as from adjacent electrochemical technologies (e.g., redox flow batteries (RFBs)), reported in the peer-reviewed literature to estimate expected value ranges of these important variables for present-day materials and cell designs. Finally, we assess the cumulative impact of all resistive losses and illustrate how the model can be used to explore pathways for reducing energy needs. Overall, this model can provide further insights into how different sources of system irreversibility may contribute to the energy requirements for separation, while also highlighting pathways to reducing energetic penalties and helping to develop engineering guidelines for molecular and system design. While we focus on a four-stage configuration with a direct capture chemistry, the methodologies presented here can be generalized to other system formats.

2. MODELING FRAMEWORK

2.1 Overview of the Modeling Framework

The model presented here describes an electrochemical reactor within a four-stage system (Figure 1a). Specifically, we consider a dissolved capture species (R) that undergoes two sequential electron transfer steps, forming a dianion (R^{2-}) that can bind one CO_2 molecule (i.e., 1 CO_2 per 2 e^-). This mechanism is representative of several weakly complexing redox-active capture molecules in literature, including tetrachloro-1,4-benzoquinone, 2,7-dichloro-1,4-benzoquinone, 2-chloro-9,10-anthraquinone, and 2,3-dichloro-1,4-naphthoquinone.[41] While a simplified reaction mechanism is shown in Figure 1a, the model considers four heterogeneous, one-electron transfer reactions that may occur in the electrochemical cell.

$$R + e^- \rightleftharpoons R^- \quad (2)$$

$$R^- + e^- \rightleftharpoons R^{2-} \quad (3)$$

$$R(CO_2) + e^- \rightleftharpoons R(CO_2)^- \quad (4)$$

$$R(CO_2)^- + e^- \rightleftharpoons R(CO_2)^{2-} \quad (5)$$

While all four reactions can occur on both electrodes; due to the reaction mechanism contemplated (i.e., weakly complexing capture species), specific subsets of reactions are expected to contribute the greatest current fraction on either electrode. At the cathode, the reactions shown in Equations 2 and 3 are anticipated to dominate. This is because the capture molecule has a low binding affinity for CO_2 in its neutral and anion states (due to the assumed weakly complexing mechanism), and therefore, concentrations of $R(CO_2)$ and $R(CO_2)^-$ are low. At the anode, the reactions shown in Equations 2, 4, and 5 may all be important. The oxidation of $R(CO_2)^{2-}$ will occur first to form $R(CO_2)^-$ (Equation 5). This may lead to the release of CO_2, followed by the oxidation of R^- (Equation 2). However, depending on the CO_2 release kinetics and/or properties that impact the

equilibrium of this reaction, the oxidation of $R(CO_2)^-$ (Equation 4) may also occur to a significant extent and, in some situations, may even be the dominant reaction.

As indicated above, homogeneous chemical reactions may also occur within the electrochemical cell. In the anodic half-cell, the release of CO_2 may occur as the capture species is deactivated via oxidation. In the cathodic half-cell, binding of CO_2 with the reduced/activated capture species can occur due to its finite solubility in the electrolyte. Further, comproportionation (or disproportionation) reactions may occur between chemical species of different (or similar) oxidation numbers. Therefore, in addition to the heterogeneous, electron-transfer reactions, we also consider homogeneous reactions within the model (i.e., CO_2 binding/release and capture species comproportionation/disproportionation). These reactions and their associated equilibrium constants, K, are shown below where Equations 6–8 represent the CO_2 binding/release reactions and Equations 9–12 represent the comproportionation/disproportionation reactions.

$$R + CO_2 \rightleftharpoons R(CO_2) \qquad K_{CO_2,1} = \frac{\left(\frac{C_{R(CO_2)}}{C_0}\right)}{\left(\frac{C_R}{C_0}\right)\left(\frac{C_{CO_2}}{C_0}\right)} \qquad 6$$

$$R^- + CO_2 \rightleftharpoons R(CO_2)^- \qquad K_{CO_2,2} = \frac{\left(\frac{C_{R(CO_2)^-}}{C_0}\right)}{\left(\frac{C_{R^-}}{C_0}\right)\left(\frac{C_{CO_2}}{C_0}\right)} \qquad 7$$

$$R^{2-} + CO_2 \rightleftharpoons R(CO_2)^{2-} \qquad K_{CO_2,3} = \frac{\left(\frac{C_{R(CO_2)^{2-}}}{C_0}\right)}{\left(\frac{C_{R^{2-}}}{C_0}\right)\left(\frac{C_{CO_2}}{C_0}\right)} \qquad 8$$

$$R + R^{2-} \rightleftharpoons 2R^- \qquad K_{comp,1} = \frac{\left(\frac{C_{R^-}}{C_0}\right)^2}{\left(\frac{C_R}{C_0}\right)\left(\frac{C_{R^{2-}}}{C_0}\right)} \qquad 9$$

$$R(CO_2) + R(CO_2)^{2-} \rightleftharpoons 2R(CO_2)^- \qquad K_{comp,2} = \frac{\left(\frac{C_{R(CO_2)^-}}{C_0}\right)^2}{\left(\frac{C_{R(CO_2)}}{C_0}\right)\left(\frac{C_{R(CO_2)^{2-}}}{C_0}\right)} \equiv \frac{K_{CO_2,2}^2 K_{comp,1}}{K_{CO_2,1} K_{CO_2,3}} \qquad 10$$

$$\mathrm{R} + \mathrm{R(CO_2)^{2-}} \rightleftharpoons \mathrm{R^-} + \mathrm{R(CO_2)^-} \qquad K_{\mathrm{comp},3} = \frac{\left(\frac{C_{\mathrm{R^-}}}{C_0}\right)\left(\frac{C_{\mathrm{R(CO_2)^-}}}{C_0}\right)}{\left(\frac{C_{\mathrm{R}}}{C_0}\right)\left(\frac{C_{\mathrm{R(CO_2)^{2-}}}}{C_0}\right)} \equiv \frac{K_{\mathrm{CO_2},2} K_{\mathrm{comp},1}}{K_{\mathrm{CO_2},3}} \qquad 11$$

$$\mathrm{R(CO_2)} + \mathrm{R^{2-}} \rightleftharpoons \mathrm{R^-} + \mathrm{R(CO_2)^-} \qquad K_{\mathrm{comp},4} = \frac{\left(\frac{C_{\mathrm{R^-}}}{C_0}\right)\left(\frac{C_{\mathrm{R(CO_2)^-}}}{C_0}\right)}{\left(\frac{C_{\mathrm{R(CO_2)}}}{C_0}\right)\left(\frac{C_{\mathrm{R^{2-}}}}{C_0}\right)} \equiv \frac{K_{\mathrm{CO_2},2} K_{\mathrm{comp},1}}{K_{\mathrm{CO_2},1}} \qquad 12$$

C_j represents the concentration of species j (mol m^{-3}). We treat the liquid electrolyte as an ideal solution, such that the activity coefficient is 1 and the species activities are equivalent to the molar concentrations relative to the standard concentration, C_0 (1000 mol m^{-3}). Note that the equilibrium constants for three of the comproportionation reactions ($K_{\mathrm{comp},2}$, $K_{\mathrm{comp},3}$, and $K_{\mathrm{comp},4}$) are not independent and, accordingly, their relationships to the other equilibrium constants are also shown.

We assume the electrochemical transformations (and any accompanying homogeneous reactions) occur within a series of electrochemical cells, each operating at the same constant current density (Figure 1b). Furthermore, we assume the number of cells in this series approaches infinity ($N \rightarrow \infty$) such that species concentrations and the electrode potential curves can be represented as continuous functions. For this analysis, we do not consider pressure losses throughout the series of cells as we seek to provide lower bound estimates of energy requirements. We also assume that the membrane/separator implemented in each cell is perfectly selective, preventing any crossover of the active species or CO_2. The series of cells is modeled as a pair of ideal packed bed reactors (PBRs), representing the series of porous cathodes and anodes, to predict concentration changes and electrode potential profiles (Figure 1c). We assume that a stagnant, concentration boundary layer (BL) is formed adjacent to the solid electrode surface as the liquid electrolyte passes through the electrode pores. While this is a simplification of typical reactor architectures, such treatments still capture important features of electrochemical cell behavior.[42,43] Accordingly, this model offers a general means of assessing performance trends and identifying

key variables with the benefit of reduced computational complexity. We provide an overview of the governing equations in the subsequent sections. A full list of the equations, and associated derivations, are included in Sections S1–S3 of the Supporting Information (SI).

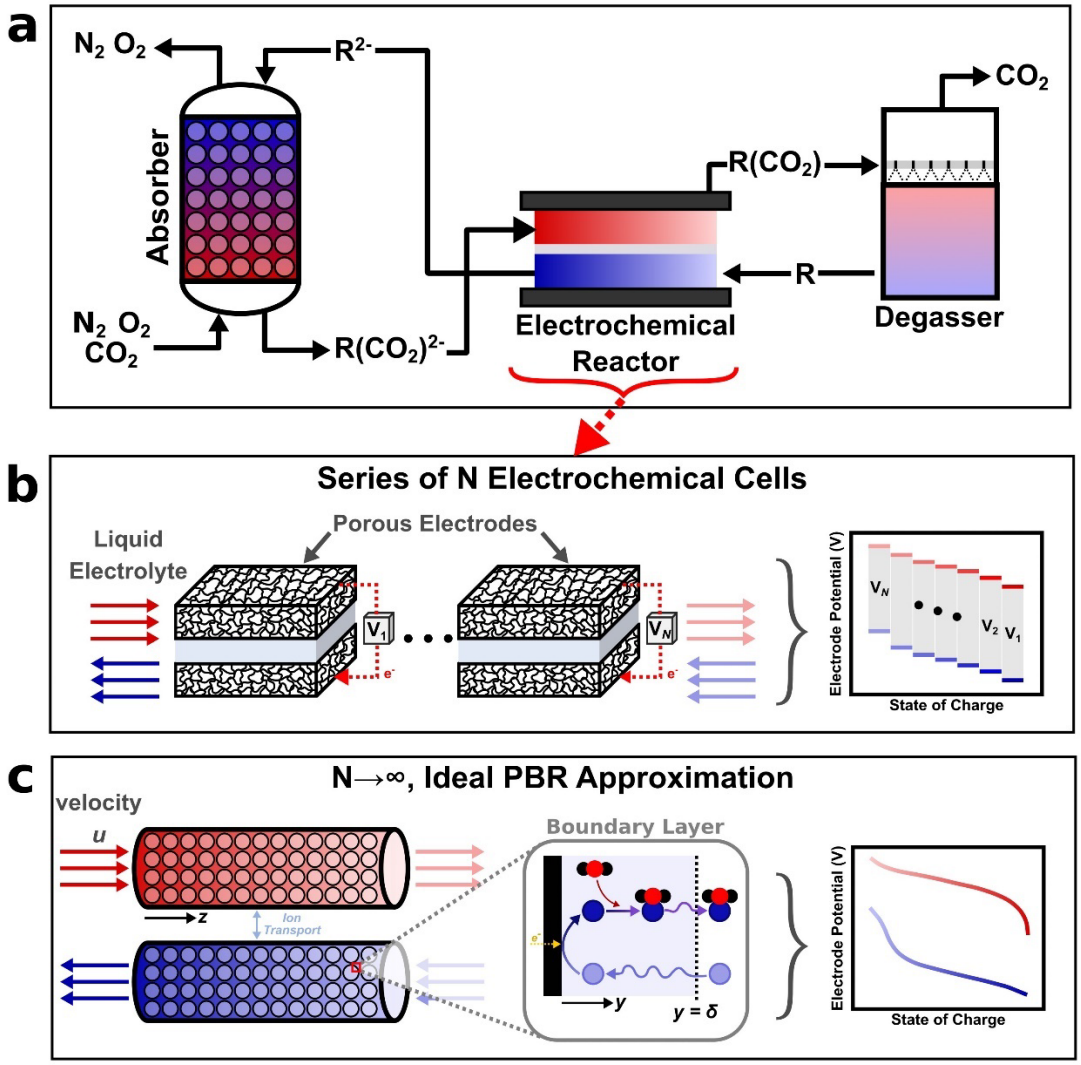

Figure 1. Overview of the electrochemical CO_2 separation system and modeling approach. (a) An illustration of the four-stage configuration based on a recirculating electrolyte containing dissolved redox-active capture species. (b) The electrochemical reactor is approximated as a series of electrochemical cells that drive the electrochemical transformations. Each individual cell consists of two porous electrodes (an anode and a cathode) with a membrane/separator between them. (c) As the numbers of cells in the series approaches infinity, the reactor can be treated as two idealized packed bed reactors (PBRs), based on the series of cathodes and anodes, with continuous potential

curves. As the bulk solution flows through the PBRs, concentration boundary layers (BLs) are formed along the surface of the solid electrodes. The BL is assumed to be stagnant, planar, and 1D. The boundary layer diagram is illustrative of the reduction reactions and any accompanying CO_2 binding that may occur during the cathodic activation step. The model captures diffusive transport, heterogeneous (electrochemical) reactions, and homogeneous reactions within this stagnant BL region. The model also represents the ohmic overpotential associated with ionic current flow between the two PBR electrodes. Here, we assume the membrane/separator is only permeable to the cationic supporting salt species.

2.2 Material Balances

2.2.1 Bulk Solution

The mole balance for each species, i, in the bulk electrolyte solution for both the series of cathodes and anodes can be generally represented by the following equation, which describes changes in bulk concentration for each species (C_i^{∞}) along the length of the reactor (z).

$$u_{\mathrm{p}} \frac{dc_i^{\infty}}{dz} = \sum s_{i,j} r_j^{\mathrm{h},\infty} - a_{\mathrm{v}} f_i^{*} \qquad 13$$

Here, u_{p} is the electrolyte velocity through the electrode pores (m s^{-1}), $r_j^{\mathrm{h},\infty}$ is the rate of homogeneous reaction j expressed using bulk concentrations (mol m^{-3} s^{-1}), and $s_{i,j}$ is the stoichiometric coefficient of species i in homogeneous reaction j (-). For $s_{i,j}$, reactants are represented with a negative value and products with a positive value. The last term in Equation 13 couples the bulk region to the BL region, where a_{v} is the total electrode surface area (and thus BL/bulk interfacial area) per electrode volume (m^2 m^{-3}) and f_i^{*} is the molar flux of species i exiting the bulk region and entering the BL region (mol m^{-2} s^{-1}). The "$*$" superscript denotes that this flux value is determined from BL concentrations. The BL equations are detailed in Section 2.2.2 and the homogeneous reaction rates are defined in Section 2.3.2.

The material balance expression described above is subject to an inlet condition. To define these inlet concentrations, we first assume that the electrolyte enters the reactor at some inlet state of charge, $x_{\mathrm{a,in}}$, where the state of charge, x_{a}, is generally defined as follows.

$$x_{\mathrm{a}} = \frac{C_{\mathrm{R}^-} + C_{\mathrm{R(CO_2)}^-} + 2C_{\mathrm{R}^{2-}} + 2C_{\mathrm{R(CO_2)}^{2-}}}{C_{\mathrm{tot}}} \quad 14$$

Here, C_{tot} represents the total capture species concentration: $C_{\mathrm{tot}} = C_{\mathrm{R}} + C_{\mathrm{R(CO_2)}} + C_{\mathrm{R}^-} + C_{\mathrm{R(CO_2)}^-} + C_{\mathrm{R}^{2-}} + C_{\mathrm{R(CO_2)}^{2-}}$. We assume that C_{tot} is conserved (i.e., there are no phase changes or side reactions leading to degradation). Then, we assume that phase equilibrium is achieved in the absorption/desorption units, meaning the concentration of dissolved CO_2 in the electrolyte entering the cathodic half-cell and the anodic half-cell is equal to $H_{\mathrm{CO_2}} P_{\mathrm{CO_2,feed}}$ and $H_{\mathrm{CO_2}} P_0$, respectively. This is in accordance with Henry's Law, where $H_{\mathrm{CO_2}}$ is the Henry's constant for CO_2 in the electrolyte solution (mol m^{-3} Pa^{-1}). We further assume that the homogeneous reactions reach equilibrium within the absorption/desorption units according to the equilibrium constants described in Equations 6–12. Overall, the defined CO_2 concentration and state of charge at the inlet, as well as the conservation of C_{tot} and four of the equilibrium constants in Equations 6–12 are used to determine inlet concentrations.

2.2.2 Boundary Layer Solution

Within BL, the mole balance for each species, i, is represented by the following equation, which describes concentration changes through the thickness of a stagnant BL (y) due to diffusion and bulk homogeneous reactions.

$$0 = D_i \frac{d^2 C_i^*}{dy^2} + \sum s_{i,j} r_j^{\mathrm{h},*} \quad 15$$

Here, C_i^* is the concentration of species i in the BL (mol m^{-3}), D_i is the diffusion coefficient of species i (m^2 s^{-1}), $s_{i,j}$ is the stoichiometric coefficient of species i in homogeneous reaction j (-), and $r_j^{h,*}$ is the rate of homogeneous reaction j expressed using BL concentrations (mol m^{-3} s^{-1}). Similar to the bulk solution equations (described in Section 2.2.1), we note that $s_{i,j}$ is positive for reactants and negative for products. The homogeneous reaction rate terms ($r_j^{h,*}$) are further defined in Section 2.3.2. Additionally, the "0" on the left-hand side of Equation 15 represents an assumption of steady-state. We also assume that the capture species diffusivities are the same in each of its different states, such that $D_R = D_{R(CO_2)} = D_{R^-} = D_{R(CO_2)^-} = D_{R^{2-}} = D_{R(CO_2)^{2-}}$. Accordingly, we generally refer to the diffusivity of the capture molecule in all states as D_R.

Solving Equation 15 requires two boundary conditions: one at the electrode surface ($y = 0$) and one at the interface between the bulk region and the BL region ($y = \delta$, where δ is the BL thickness). At $y = \delta$, the BL concentrations are equivalent to the bulk values (C_i^∞, as solved for with Equation 13). At the electrode surface, $y = 0$, the molar flux of species i is set equal to the rate of the electrochemical reaction. Both boundary conditions are defined as follows.

$$C_i^*|_{y=\delta} = C_i^\infty \quad (16)$$

$$-D_i \left.\frac{dC_i^*}{dy}\right|_{y=0} = \sum s_{i,k} r_k^e \quad (17)$$

Here, $s_{i,k}$ is the stoichiometric coefficient of species i in electrochemical reaction k (-) and r_k^e is the rate of electrochemical reaction k (mol m^{-2} s^{-1}). For the electrochemical reactions, which are defined in the reduction direction (Equations 2–5), $s_{i,k}$ is defined here to be negative for reactants (more oxidized species) and positive for products (more reduced species) The electrochemical reaction rate terms are detailed in Section 2.3.1.

The molar flux term (f_i^*) introduced in Equation 13 is determined from the BL concentration profiles, as defined below.

$$f_i^* = D_i \left.\frac{dC_i^*}{dy}\right|_{y=\delta} \quad 18$$

This expression in combination with Equation 16, effectively link the bulk and BL equations.

2.3 Reaction Rates

2.3.1 Heterogeneous (Electrochemical) Reaction Rates

The rate of each electrochemical reaction k (r_k^{e}) is proportional to the local, surface-normal current density supporting that reaction ($i_{\mathrm{n},k}$). Rate expressions for the four possible electrode reactions considered are shown below.

$\mathrm{R/R^-}$ couple: $r_1^{\mathrm{e}} = \frac{i_{\mathrm{n},1}}{F}$ 19

$\mathrm{R^-/R^{2-}}$ couple: $r_2^{\mathrm{e}} = \frac{i_{\mathrm{n},2}}{F}$ 20

$\mathrm{R(CO_2)/R(CO_2)^-}$ couple: $r_3^{\mathrm{e}} = \frac{i_{\mathrm{n},3}}{F}$ 21

$\mathrm{R(CO_2)^-/R(CO_2)^{2-}}$ couple: $r_4^{\mathrm{e}} = \frac{i_{\mathrm{n},4}}{F}$ 22

Here, F is the Faraday constant (96485 C mol^{-1}). Generally, these reactions can be denoted as $r_k^{\mathrm{e}} = i_{\mathrm{n},k}/nF$ where n (the number of electrons transferred) is equal to 1 here. Accordingly, since the number of electrons transferred is 1 in the considered electrochemical reactions, n is dropped from subsequent equations (i.e., Butler-Volmer equation and Nernst equation). We note that the surface-normal current densities for each reaction must sum to the overall operating surface-normal current density (i_{n}).

$$i_{\mathrm{n},1} + i_{\mathrm{n},2} + i_{\mathrm{n},3} + i_{\mathrm{n},4} = i_{\mathrm{n}} \quad 23$$

We assume that the kinetics of the electrochemical reactions can be described by the Butler-Volmer formalism. Accordingly, the surface-normal current density of each reaction, k, is related to the activation overpotential ($\eta_{\mathrm{act},k}$) and the exchange current density ($i_{0,k}$) for that specific reaction as shown below.

$$i_{\mathrm{n},k} = i_{0,k}\left(\exp\left(\frac{\alpha_{\mathrm{a},k}F}{R_{\mathrm{u}}T}\eta_{\mathrm{act},k}\right) - \exp\left(\frac{-\alpha_{\mathrm{c},k}F}{R_{\mathrm{u}}T}\eta_{\mathrm{act},k}\right)\right) \quad (24)$$

$\alpha_{\mathrm{a},k}$ and $\alpha_{\mathrm{c},k}$ (-) are the charge transfer coefficients in the oxidative/anodic and reductive/cathodic directions, respectively, for each reaction. The activation overpotential, η_{act}, is further defined in Section 2.4.3. The exchange current density, i_0 (A m^{-2}), can be expressed as a function of the heterogeneous rate constant, k_0 (m s^{-1}), and the reactant/product concentrations adjacent to the electrode surface (C_i^{s}, defined at $y = 0$ in the BL).

$$i_{0,k} = k_{0,k}F\left(C_{\mathrm{red},k}^{\mathrm{s}}\right)^{\alpha_{\mathrm{c},k}}\left(C_{\mathrm{ox},k}^{\mathrm{s}}\right)^{1-\alpha_{\mathrm{c},k}} \quad (25)$$

Here, the subscript "red, k" represents the reduced species and "ox, k" represents the oxidized species, respectively, in electrochemical reaction k.

2.3.2 Homogeneous Reaction Rates

The homogeneous CO_2 binding rate expressions ($r_{\mathrm{b}}^{\mathrm{h}}$) are defined as follows.

$$r_{\mathrm{b},1}^{\mathrm{h}} = k_{\mathrm{bind},1}C_{\mathrm{R}}C_{\mathrm{CO_2}} - k_{\mathrm{rel},1}C_{\mathrm{R(CO_2)}} \qquad \frac{K_{\mathrm{CO_2},1}}{C_0} = \frac{k_{\mathrm{bind},1}}{k_{\mathrm{rel},1}} \quad (26)$$

$$r_{\mathrm{b},2}^{\mathrm{h}} = k_{\mathrm{bind},2}C_{\mathrm{R^-}}C_{\mathrm{CO_2}} - k_{\mathrm{rel},2}C_{\mathrm{R(CO_2)^-}} \qquad \frac{K_{\mathrm{CO_2},2}}{C_0} = \frac{k_{\mathrm{bind},2}}{k_{\mathrm{rel},2}} \quad (27)$$

$$r_{\mathrm{b},3}^{\mathrm{h}} = k_{\mathrm{bind},3}C_{\mathrm{R^{2-}}}C_{\mathrm{CO_2}} - k_{\mathrm{rel},3}C_{\mathrm{R(CO_2)^{2-}}} \qquad \frac{K_{\mathrm{CO_2},3}}{C_0} = \frac{k_{\mathrm{bind},3}}{k_{\mathrm{rel},3}} \quad (28)$$

Here, $k_{\mathrm{bind},1}$, $k_{\mathrm{bind},2}$, and $k_{\mathrm{bind},3}$ are the forward rate constants for the three CO_2 binding reactions (m^3 mol^{-1} s^{-1}). $k_{\mathrm{rel},1}$, $k_{\mathrm{rel},2}$, and $k_{\mathrm{rel},3}$ are the reverse rate constants for the three CO_2 binding

reactions, which can also be described as the CO_2 release rate constants (s^{-1}). For each reaction, the forward and reverse rate constants can be related to the equilibrium binding constant as shown above.

The homogeneous comproportionation rate expressions (r_c^h) are defined as follows.

$$r_{c,1}^h = k_{comp,1} C_R C_{R^{2-}} - k_{disp,1} C_{R^-}^2 \qquad K_{comp,1} = \frac{k_{comp,1}}{k_{disp,1}} \qquad 29$$

$$r_{c,2}^h = k_{comp,2} C_{R(CO_2)} C_{R(CO_2)^{2-}} - k_{disp,2} C_{R(CO_2)^-}^2 \qquad K_{comp,2} = \frac{k_{comp,2}}{k_{disp,2}} \qquad 30$$

$$r_{c,3}^h = k_{comp,3} C_R C_{R(CO_2)^{2-}} - k_{disp,3} C_{R^-} C_{R(CO_2)^-} \qquad K_{comp,3} = \frac{k_{comp,3}}{k_{disp,3}} \qquad 31$$

$$r_{c,4}^h = k_{comp,4} C_{R(CO_2)} C_{R^{2-}} - k_{disp,4} C_{R^-} C_{R(CO_2)^-} \qquad K_{comp,4} = \frac{k_{comp,4}}{k_{disp,4}} \qquad 32$$

In the above equations, $k_{comp,1}$, $k_{comp,2}$, $k_{comp,3}$, and $k_{comp,4}$ are the forward rate constants (m^3 mol^{-1} s^{-1}) and $k_{disp,1}$, $k_{disp,2}$, $k_{disp,3}$, and $k_{disp,4}$ are the reverse rate constants (m^3 mol^{-1} s^{-1}) for the four comproportionation reactions (i.e., disproportionation rate constants). For each reaction, the ratio of forward and reverse rate constants represents the equilibrium comproportionation constant as shown above. Note that the CO_2 binding and comproportionation rates outlined in Equations 26–32 can be defined in terms of either bulk or BL concentrations (C_i^∞ or C_i^*, respectively).

2.4 Cell Voltage, Electrode Potential, and Overpotentials

The voltage of each cell (V) in the series is represented by the difference in electrode potentials, plus an overpotential term representing ohmic losses of the cell (η_{ohm}).

$$V = E_{cath} - E_{an} + \eta_{ohm} \qquad 33$$

The subscripts "cath" and "an" represent the cathode and anode, respectively. We note that V will be negative since the cells are operated electrolytically (thermodynamically non-spontaneous) in this process.

The electrode potential (E) can then be represented by the summation of an equilibrium potential (E_{eq}), the concentration overpotential (η_{conc}), and the activation overpotential (η_{act}), as shown below.

$$E = E_{\mathrm{eq}}^{\infty} + \eta_{\mathrm{conc}} + \eta_{\mathrm{act}} \quad 34$$

The "∞" superscript in the equilibrium potential denotes the use of bulk species concentrations to determine this value. Under cathodic (i.e., negative) currents, the overpotentials are negative and the electrode potential is more negative than the equilibrium bulk potential. Conversely, for anodic (i.e., positive) currents, the overpotentials are positive and the electrode potential is more positive than the equilibrium bulk potential. However, these expectations may be impacted by any homogeneous reactions occurring near the electrode surface.

2.4.1 Equilibrium Potential

Under conditions of electrochemical equilibrium, the electrode potential is governed by the Nernst equation, which is defined by the following equation for each electrochemical reaction, k.

$$E_{\mathrm{eq},k} = E_{k,0} - \frac{R_{\mathrm{u}}T}{F} \ln\left(\frac{C_{\mathrm{red},k}}{C_{\mathrm{ox},k}}\right) \quad 35$$

Here, $E_{k,0}$ is the standard reduction potential of the electrochemical reaction (V vs. an arbitrary reference). As described earlier, E_{eq}^{∞} in Equation 34 is determined with the bulk species concentrations, and the effects of surface concentration are captured in the concentration

overpotential (Section 2.4.2). The standard reduction potentials are also related via functions involving the equilibrium constants, which are shown in Section S1.3.1 of the SI.

2.4.2 Concentration Overpotential

During practical operation, the electrochemical reactions (and any accompanying chemical reactions) will produce concentration gradients between the bulk solution and the solution directly adjacent to the solid electrode (i.e., across the concentration BL). The concentration overpotential, η_{conc}, can be used to characterize potential differences due to the formation of these gradients. We define η_{conc} as this potential difference between the electrode surface and the bulk solution which can be determined by the following equation for each electrochemical reaction, k.

$$\eta_{\mathrm{conc},k} = E^{s}_{\mathrm{eq},k} - E^{\infty}_{\mathrm{eq},k} = -\frac{R_{\mathrm{u}}T}{F}\ln\left(\frac{{C^{s}_{\mathrm{red},k}}/{C^{\infty}_{\mathrm{red},k}}}{{C^{s}_{\mathrm{ox},k}}/{C^{\infty}_{\mathrm{ox},k}}}\right) \tag{36}$$

The "s" subscript denotes that the value is evaluated adjacent to the electrode surface.

2.4.3 Activation Overpotential

The activation overpotential, η_{act}, is defined as the difference between the electrode potential and the equilibrium potential considering the species concentrations adjacent to the electrode surface. This is the overpotential required to overcome the activation energy of a given electrochemical reaction, k, to achieve a specified surface-normal current density, $i_{\mathrm{n},k}$. The activation overpotential for each electrochemical reaction is defined below.

$$\eta_{\mathrm{act},k} = E - E^{s}_{\mathrm{eq},k} \tag{37}$$

The relationship between the activation overpotential, the surface-normal current density, and species concentrations was described previously in Equation 24.

2.4.4 Ohmic Overpotential

We assume that the electrolyte contains excess supporting electrolyte, such that the concentration of ions in the electrolyte remains nearly constant throughout the porous membrane/separator and electrodes. Under these conditions, the effects of migration are negligible and charge transfer through the electrolyte can be described by Ohm's law. Accordingly, the ohmic overpotential, η_{ohm}, is described by Equation 38.

$$\eta_{\mathrm{ohm}} = i_{\mathrm{g}} \cdot ASR \tag{38}$$

Here, i_{g} is the geometric current density (A m^{-2}) and ASR is the area specific resistance of the cell (Ω m^2).

The i_{g} parameter considers the total current per geometric area of each electrochemical cell, and it is defined as a negative value such that $\eta_{\mathrm{ohm}} < 0$. In this study, it is assumed that each reactor in the series is operated at the same i_{g}. The geometric current density can be related to the surface normal current density with Faraday's law. Given our assumption that i_{n} is constant throughout the entire electrode, the following expression can be derived.

$$i_{\mathrm{g}} = -\frac{a_{\mathrm{v}} V_{\mathrm{elec}} |i_{\mathrm{n}}|}{A_{\mathrm{g,elec}}} = -a_{\mathrm{v}} L_{\mathrm{elec}} |i_{\mathrm{n}}| \tag{39}$$

Here, V_{elec} is the electrode volume (m^3), $A_{\mathrm{g,elec}}$ is the geometric area of the electrode (m^2), and L_{elec} is the electrode thickness (m). The absolute value of i_{n} is used as its sign is dependent on the electrode (i.e., cathode or anode).

The ASR of the cell is a summation of the ionic resistances of the membrane/separator and the electrolyte within the porous electrodes, the electronic resistances of the solid cell components (e.g., porous electrodes, current collectors, etc.), and the contact resistances between these different

components. In typical cell designs and operating regimes, the ionic resistances dominate the ASR, most often from the membrane/separator.[44,45]

2.5 Dimensionless Model & Model Simplifications

To simplify the modeling framework, physical dimensions were removed from the material balance equations. Non-dimensionalization of the governing equations helps to scale all variables from 0 to order 1, to identify key dimensionless groups that govern performance, and to decrease the number of parameters considered.[46] Here, we provide an overview of the non-dimensionalization procedure and define the derived equations. A more detailed description of this process can be found in Section S2 of the SI.

The equations were non-dimensionalized by introducing the following dimensionless variables into the governing equations and boundary conditions.

$$\tilde{C}_{\mathrm{R},i} = \frac{C_{\mathrm{R},i}}{C_{\mathrm{R,tot}}}, \quad \tilde{C}_{\mathrm{CO_2}} = \frac{C_{\mathrm{CO_2}}}{H_{\mathrm{CO_2}} P_0}, \quad \tilde{z} = \frac{Z}{L}, \quad \tilde{y} = \frac{y}{\delta}, \quad \tilde{E} = \frac{E}{R_{\mathrm{u}} T / F},$$

$$\tilde{\eta} = \frac{\eta}{R_{\mathrm{u}} T / F}, \quad \tilde{\imath}_{\mathrm{n},1} = \frac{i_{\mathrm{n},1}}{i_{\mathrm{n}}}, \quad \tilde{\imath}_{\mathrm{n},2} = \frac{i_{\mathrm{n},2}}{i_{\mathrm{n}}}, \quad \tilde{\imath}_{\mathrm{n},3} = \frac{i_{\mathrm{n},3}}{i_{\mathrm{n}}}, \quad \tilde{\imath}_{\mathrm{n},4} = \frac{i_{\mathrm{n},4}}{i_{\mathrm{n}}} \qquad 40$$

In the defined variables above, $\tilde{\imath}_{\mathrm{n},k}$ can be described as the fraction of current going towards reaction k.

With these new variables defined in Equation 40, the dimensionless BL material balance equations were first derived. The generalized forms of these equations are shown in Equations 41 and 42 for the capture species and CO_2, respectively.

$$-\frac{d^2 \tilde{C}^*_{\mathrm{R},i}}{d\tilde{y}^2} = \sum s_{i,j} \tilde{r}_j^{\mathrm{h}} \qquad 41$$

$$-\frac{d^2 \tilde{C}^*_{\mathrm{CO_2}}}{d\tilde{y}^2} = \frac{r_{\mathrm{D}}}{\tilde{H}_{\mathrm{CO_2}}} \left(\sum s_{i,j} \tilde{r}_j^{\mathrm{h}} \right) \qquad 42$$

In the above equations, r_{D} is the diffusivity ratio of the capture species to CO_2 and $\widetilde{H}_{\mathrm{CO_2}}$ is the relative CO_2 solubility. Both of these dimensionless groups are further defined in Table 1. Furthermore, $\tilde{r}_j^{\mathrm{h}}$ is the dimensionless reaction rate expression for homogenous reaction j. The generalized form used for $\tilde{r}_j^{\mathrm{h}}$ is defined by Equation 43 for reactions where the forward rate is dominant (reactions shown in Equations 8–12) and by Equation 44 where the reverse reaction is dominant (reactions shown in Equations 6 and 7).

$$\tilde{r}_j^{\mathrm{h}} = Da_j \left(\prod_i^{N_{\mathrm{R}}} \tilde{C}_i^{\ -s_{i,j}} - \frac{1}{\widetilde{K}_j} \prod_i^{N_{\mathrm{P}}} \tilde{C}_i^{\ s_{i,j}} \right) \tag{43}$$

$$\tilde{r}_j^{\mathrm{h}} = Da_j \left(\widetilde{K}_j \prod_i^{N_{\mathrm{R}}} C_i^{\ -s_{i,j}} - \prod_i^{N_{\mathrm{P}}} C_i^{\ s_{i,j}} \right) \tag{44}$$

Here, N_{R} is the number of reactants, N_{P} is the number of products, $\widetilde{K}_j$ is the re-scaled equilibrium constant of reaction j, and Da_j is the Damköhler number for reaction j. The Damköhler number describes the relative rates of reaction to diffusive mass transport, and is further defined in Table 1. The re-scaled equilibrium constants for the CO_2 binding/release reactions can be described as the gas-phase binding coefficients, and they are also further defined in Table 1. For the comproportionation/disproportionation reactions, the re-scaled equilibrium constants are equivalent to the comproportionation coefficients defined in Equations 9–12.

The generalized forms of the dimensionless boundary conditions for the boundary layer solution are as follows.

$$\tilde{C}_i^* \big|_{\tilde{y}=1} = \tilde{C}_i^{\infty} \tag{45}$$

$$-\frac{d\tilde{C}_i^*}{d\tilde{y}}\bigg|_{\tilde{y}=0} = -\gamma_{\mathrm{mt}} \sum s_{i,k} \tilde{\imath}_{\mathrm{n},k} \tag{46}$$

In the above equation, γ_{mt} is one representation of the dimensionless current density, and it is further described in Table 1. Then, the fractional currents ($\tilde{\imath}_{\mathrm{n},k}$) are further defined with the dimensionless form of the Butler-Volmer equation shown below.

$$\tilde{\imath}_{\mathrm{n},k} = \frac{\left(\tilde{C}^{\mathrm{s}}_{\mathrm{red},k}\right)^{\alpha_{\mathrm{c},k}}\left(\tilde{C}^{\mathrm{s}}_{\mathrm{ox},k}\right)^{\alpha_{\mathrm{a},k}}}{\gamma_{\mathrm{el}}}\left(\exp\left(\alpha_{\mathrm{a},k}\tilde{\eta}_{\mathrm{act}}\right) - \exp\left(-\alpha_{\mathrm{c},k}\tilde{\eta}_{\mathrm{act}}\right)\right) \quad 47$$

The derived γ_{el} parameter is another form of the dimensionless current density which is also defined in Table 1. This variable can be defined in terms of γ_{mt} as such: $\gamma_{\mathrm{el}} = \gamma_{\mathrm{mt}}/\lambda$. The λ parameter is the intrinsic rate of the electrochemical reaction relative to the rate of mass transport, and it is defined in Table 1 and discussed further in Section 3.3.

For the bulk solution, the dimensionless material balance equations for the capture species and CO_2 are defined in Equations 48 and 49, respectively.

$$\frac{d\tilde{C}^{\infty}_{\mathrm{R},i}}{d\tilde{z}} = \omega\left(\sum s_{i,j}\tilde{r}^{\mathrm{h}}_{j}\right) - \frac{2\Delta x_{\mathrm{a}}}{|\gamma_{\mathrm{mt}}|}\left(\left.\frac{d\tilde{C}^{*}_{\mathrm{R},i}}{d\tilde{y}}\right|_{\tilde{y}=1}\right) \quad 48$$

$$\frac{d\tilde{C}^{\infty}_{\mathrm{CO_2}}}{d\tilde{z}} = \frac{\omega}{\tilde{H}_{\mathrm{CO_2}}}\left(\sum s_{i,j}\tilde{r}^{\mathrm{h}}_{j}\right) - \frac{2\Delta x_{\mathrm{a}}}{|\gamma_{\mathrm{mt}}|}\frac{1}{r_{\mathrm{D}}}\left(\left.\frac{d\tilde{C}^{*}_{\mathrm{CO_2}}}{d\tilde{y}}\right|_{\tilde{y}=1}\right) \quad 49$$

The derived ω parameter represents the ratio of the reactor time scale (i.e., residence time, τ) to the diffusion time scale. Then, Δx_{a} is the state of charge swing, which is the difference in state of charge between the inlet and outlet of the electrochemical reactor. We note that Δx_{a} is identical for the cathode and anode PBR reactors. Both ω and Δx_{a} are defined in Table 1. Additionally, the derivation of the $2\Delta x_{\mathrm{a}}/|\gamma_{\mathrm{mt}}|$ term in Equations 48 and 49 is detailed in Section S2.2.3 of the SI.

The dimensionless inlet condition for the bulk solution is shown in Equation 50.

$$\left.\tilde{C}^{\infty}_{i}\right|_{\tilde{z}=0} = \tilde{C}^{\mathrm{in}}_{i} \quad 50$$

The "in" subscript denotes inlet concentration. For CO_2, $\tilde{C}^{\mathrm{in}}_{\mathrm{CO_2}} = \tilde{P}_{\mathrm{CO_2,feed}}$ for the cathode inlet and $\tilde{C}^{\mathrm{in}}_{\mathrm{CO_2}} = 1$ for the anode inlet. $\tilde{P}_{\mathrm{CO_2,feed}}$ is the dimensionless partial pressure of CO_2 in the feed gas

($\tilde{P}_{\mathrm{CO_2,feed}} = P_{\mathrm{CO_2,feed}}/P_0$). Then, with the dimensionless inlet CO_2 concentration defined, the inlet concentrations of the other species can be determined by assuming a state of equilibrium according to the equilibrium constants in Equations 6–12, and by assuming an inlet state of charge.

Finally, the equations defining the dimensionless equilibrium potential and overpotentials are shown in Equations 51–54.

$$\tilde{E}_{\mathrm{eq},k} = \tilde{E}_{k,0} - \ln\left(\frac{\tilde{C}_{\mathrm{red},k}}{\tilde{C}_{\mathrm{ox},k}}\right) \quad 51$$

$$\tilde{\eta}_{\mathrm{conc},k} = \tilde{E}^{\mathrm{s}}_{\mathrm{eq},k} - \tilde{E}^{\infty}_{\mathrm{eq},k} = -\ln\left(\frac{\tilde{C}^{\mathrm{s}}_{\mathrm{red},k}/\tilde{C}^{\infty}_{\mathrm{red},k}}{\tilde{C}^{\mathrm{s}}_{\mathrm{ox},k}/\tilde{C}^{\infty}_{\mathrm{ox},k}}\right) \quad 52$$

$$\tilde{\eta}_{\mathrm{act},k} = \tilde{E} - \tilde{E}^{\mathrm{s}}_{\mathrm{eq},k} \quad 53$$

$$\tilde{\eta}_{\mathrm{ohm}} = -\sigma|\gamma_{\mathrm{mt}}| \quad 54$$

In the dimensionless ohmic overpotential (Equation 54), σ is the ratio of the ohmic resistance to the mass transport resistance in the boundary layer. This parameter is defined in Table 1 and further discussed in Section 3.5.

To streamline the subsequent analyses in this work, we make several important assumptions. We assume that the heterogeneous rate constant (denoted as k_0) is equivalent for each of the electrochemical reactions and the charge transfer coefficients (α) are identical for each electrochemical reaction and are of equal magnitude for the anodic and cathodic reactions. Furthermore, we limit our analyses to two bounding cases for the cell model. In the first case, we assume fast homogeneous kinetics such that each homogeneous reaction reaches equilibrium at all points ($Da_j >> 1$). In the second case, we assume slow homogeneous reactions such that $Da_j = 0$. In these two cases, the governing equations can be simplified as outlined in Section S3 of the SI.

Table 1. Definitions of dimensionless parameters and groupings.

Parameter	Definition	Equation
γ_{mt}	$\frac{\text{Reaction rate (electrochemical)}}{\text{Mass transport rate in the BL}}$	$\frac{i_{\mathrm{n}}\delta}{FD_{\mathrm{R}}C_{\mathrm{R,tot}}}$
γ_{el}	$\frac{\text{Reaction rate (electrochemical)}}{\text{Intrinsic electrochemical reaction rate}}$	$\frac{i_{\mathrm{n}}}{k_0FC_{\mathrm{R,tot}}}$
Da	$\frac{\text{Reaction rate (homogenoeus)}}{\text{Mass transport rate in the BL}}$	$\frac{k_{\mathrm{bind}}\delta^2H_{\mathrm{CO_2}}P_0}{D_{\mathrm{R}}}$ or $\frac{k_{\mathrm{rel}}\delta^2}{D_{\mathrm{R}}}$ or $\frac{k_{\mathrm{comp}}\delta^2C_{\mathrm{R,tot}}}{D_{\mathrm{R}}}$
ω	$\frac{\text{Reactor residence time}}{\text{BL mass transport time scale}}$	$\frac{\tau D_{\mathrm{R}}}{\delta^2}$
σ	$\frac{\text{Ohmic resistance}}{\text{BL mass transport resistance}}$	$\frac{F^2a_{\mathrm{v}}D_{\mathrm{R}}L_{\mathrm{elec}}C_{\mathrm{R,tot}}ASR}{\delta R_{\mathrm{u}}T}$
λ	$\frac{\text{Intrinsic electrochemical reaction rate}}{\text{BL mass transport resistance}}$	$\frac{\delta k_0}{D_{\mathrm{R}}}$
$K_{\mathrm{CO_2(g),1}}$	R binding constant defined for gas-phase CO_2	$\frac{H_{\mathrm{CO_2}}P_0}{C_0}K_{\mathrm{CO_2,1}}$
$K_{\mathrm{CO_2(g),2}}$	R^- binding constant defined for gas-phase CO_2	$\frac{H_{\mathrm{CO_2}}P_0}{C_0}K_{\mathrm{CO_2,2}}$
$K_{\mathrm{CO_2(g),3}}$	R^{2-} binding constant defined for gas-phase CO_2	$\frac{H_{\mathrm{CO_2}}P_0}{C_0}K_{\mathrm{CO_2,3}}$
$\tilde{H}_{\mathrm{CO_2}}$	Relative CO_2 Solubility	$\frac{H_{\mathrm{CO_2}}P_0}{C_{\mathrm{R,tot}}}$
r_{D}	Diffusivity ratio	$\frac{D_{\mathrm{R}}}{D_{\mathrm{CO_2}}}$
Δx_{a}	State of charge swing	$\left(x_{\mathrm{a,out}} - x_{\mathrm{a,in}}\right)_{\mathrm{cath}} \equiv \left(x_{\mathrm{a,in}} - x_{\mathrm{a,out}}\right)_{\mathrm{an}}$

2.6 Quantifying Separated CO_2 & Work

The amount of CO_2 captured and released is quantified using the difference in total CO_2 in solution after absorption (anode PBR inlet) and after desorption (cathode PBR inlet). Here, we consider the normalized quantity of total CO_2 in solution, $x_{\mathrm{CO_2}}$, which is defined as follows.

$$x_{\mathrm{CO_2}} = \tilde{C}_{\mathrm{R(CO_2)}} + \tilde{C}_{\mathrm{R(CO_2)^-}} + \tilde{C}_{\mathrm{R(CO_2)^{2-}}} + \tilde{H}_{\mathrm{CO_2}}\tilde{C}_{\mathrm{CO_2}} \quad 55$$

Here, we consider the work (W) required to operate the electrochemical cell in the four-stage system configuration. Under the assumption that the electrochemical process step occurs over an infinite series of cells, with each operating with an infinitely small state of charge swing, W can be determined by taking the path integral of electrode potential, E, vs the state of charge, x_{a}, with an added penalty to represent the ohmic resistance of the separator/membrane between the electrodes. The equation for W is shown in the following equation.

$$W = \frac{2F \oint E \, dx_{\mathrm{a}}}{\Delta x_{\mathrm{CO_2}}} + \frac{2F\eta_{\mathrm{ohm}}\Delta x_{\mathrm{a}}}{\Delta x_{\mathrm{CO_2}}} \quad 56$$

In the above equation, the 2 represents that this is an overall two-electron transfer process between the activated and deactivated states of the capture molecule. Then, $\Delta x_{\mathrm{CO_2}}$ represents the difference in $x_{\mathrm{CO_2}}$ entering the anode PBR reactor (after absorption) and entering the cathode PBR reactor (after desorption). The path considered for the above E vs x_{a} path integral is defined as follows: (1) cathode PBR inlet → (2) cathode PBR outlet → (3) anode PBR inlet → (4) anode PBR outlet → (1) cathode PBR inlet. We also note that in our evaluations throughout Section 3, we use an electrode potential deviation, $E - E_{1,0}$, in our work calculations rather than the electrode potential, E. This does not impact work calculations as the standard reduction potential, $E_{1,0}$, is a constant value. For brevity, we refer to $E - E_{1,0}$ as the electrode potential throughout our discussions.

2.7 Computational Resources & Methods

In this modeling framework, the governing equations were solved using MATLAB R2022b. For the limiting case of $Da \to \infty$ (equilibrium homogeneous reactions), a system of nonlinear equations had to be solved at each point along the length of the reactor, z, to determine the species concentrations throughout the bulk and BL regions. For the equilibrium concentrations, there is a

set of seven equations with seven unknown concentrations. Through a method of substitution, this was rearranged into one nonlinear equation with one unknown (as described in Section S3.1 of the SI). This equation was solved using the built-in *fzero* function. After solving for the concentrations, the values were used to determine fractional currents, overpotentials, equilibrium potentials, and the work. For the case of $Da = 0$, concentrations and fractional currents were solved simultaneously. The bulk material balances were defined as a function of ordinary differential equations (ODEs) that were solved using the built-in *ode15s* function. Within the function defining the ODEs, there is a call to a separate user-defined function to solve for the surface concentrations and the fractional currents at each incremental length along the PBRs. This is required to solve for the species derivative terms used to define fluxes between the bulk and BL, $\left.\frac{d\tilde{C}_j^*}{d\tilde{y}}\right|_{\tilde{y}=1}$, which appear in the bulk material balance equations. First, to solve for the fractional currents, a system of nonlinear equations is derived (as described in Section S3.2 of the SI) and solved using the built-in *fsolve* function. Then, the fractional currents are used to determine BL concentrations. The BL concentration profiles are used to define the BL/bulk fluxes (as described above) and enable solving the material balances for the bulk concentrations. The resolved concentrations (both bulk and BL) and fractional currents are used to determine overpotentials, equilibrium potentials, and work. The simulations in this work were performed using a Dell Latitude 7290 laptop with an Intel® Core™ i7-8650U Processor (CPU @ 1.90 GHz, 4 Cores, 8 Logical Processors). Each individual simulation took ~1–20 s.

3. RESULTS & DISCUSSION

Using the derived electrochemical reactor model, we evaluate and compare energetic penalties from internal and external irreversibilities within the cells due to mass transport, electrochemical

kinetics, homogeneous kinetics, and ohmics. We independently explore each of the key dimensionless variables associated with these phenomena across a range of relevant values, and then evaluate their cumulative impact on the overall energy requirements. For this analysis, we specifically consider a separation scenario where CO_2 is captured from a 15 mol% feedstock and recovered as a pure product (100 mol% CO_2). This is representative of flue gas compositions in post-combustion capture from coal-fired power plants.[31] For the base case, we assume the following parameter values: $\Delta E_0 = E_{1,0} - E_{2,0}$ = 0.85 V, Δx_a = 0.8, $\widetilde{H}_{CO_2}$ = 0.1, r_D = 0.5, $K_{CO_2(g),1}$ = 10^{-4}, $K_{CO_2(g),2}$ = 10^{-3}, and $K_{CO_2(g),3}$ = 7320. This selection is based on current electrolyte formulations in the field, which typically comprise quinone capture molecules dissolved in nonaqueous electrolytes.[47] A ΔE_0 value of 0.85 V is based on the average value of several quinones reported by Simeon et al.[41] A relative CO_2 solubility, $\widetilde{H}_{CO_2}$, of 0.1 is representative of electrolytes based on propylene carbonate or dimethylsulfoxide solvents, which have a CO_2 solubility of ca. 0.1 M atm^{-1},[48] and a capture species concentration of 1 M. A diffusivity ratio, r_D, of 0.5 was also selected based on reported diffusivity values of quinones and CO_2 in nonaqueous solvents. The relative diffusivity of quinone to CO_2 in such solvents is generally in the range of ca. 0.1–1.[49–53] The binding coefficient of the dianionic species, $K_{CO_2(g),3}$, was selected based on (1) reported values for $K_{CO_2,3}$ in molecules that undergo weakly-complexing mechanisms,[41] and (2) an assumed H_{CO_2} value of 0.1 M atm^{-1}. Then, the binding coefficients of the neutral and anionic states of the molecule, $K_{CO_2(g),1}$ and $K_{CO_2(g),2}$, were set to values $\ll$ 1 to reflect the assumed weakly-complexing mechanism.

We vary some of these base case parameters throughout the Results & Discussion section to explore their impact on system performance. The chosen set of parameters allows for up to >99.9%

capture of CO_2, which is greater than the typical 90% threshold.[8,33] However, for this analysis, we assume that the system is used to capture 90% of CO_2 from the feed gas which sets the minimum work of separation to 6.4 kJ (mol CO_2)$^{-1}$. This impacts the quantification of the energetic penalty from external irreversibilities (described in Section 3.1). However, if a higher capture fraction were chosen, the minimum work would only change by < 1 kJ (mol CO_2)$^{-1}$, and therefore, would not significantly impact the analysis.

3.1 Thermodynamic Cycle & External Irreversibilities

Representing the electrochemical CO_2 separation system as an ideal thermodynamic cycle provides information about the minimum energy requirements, including $W_{\min}$ and energetic penalties associated with external irreversibilities. This approach has been previously employed for different configurations of electrochemical systems with mobile capture species.[32,34,35] We employ the same approach here; however, we note that these previous analyses were conducted assuming concerted electron transfer mechanisms, whereas here we assume sequential electron transfer events, which is more aligned with the recent literature.[41] To conduct this thermodynamic analysis, we assume all electrochemical and chemical reactions are at equilibrium within the cell. For the electrode reactions, this means that Nernstian kinetics apply ($\gamma_{\mathrm{el}} \to 0$), where the electrode potentials are represented by the Nernst equation (Equation 35 or 51) rather than the Butler-Volmer equation (Equation 24 or 47). We also assume that the surface concentrations approach the bulk concentrations ($\gamma_{\mathrm{mt}} \to 0$).

Figure 2 demonstrates the thermodynamic cycle for a four-stage system using the base case set of material and system properties. The first stage of the cycle is defined as cathodic activation, where the capture molecule is electrochemically reduced and thus activated for CO_2 binding. The

first plateau region represents the $R + e^- \rightarrow R^-$ reaction. Then, as the subsequent electron transfer reaction ($R^- + e^- \rightarrow R^{2-}$) begins, the potential sharply decreases. The shoulder before the second plateau region is caused by the binding reaction with CO_2 dissolved in electrolyte solution, $R^{2-} + CO_2 \rightarrow R(CO_2)^{2-}$, which removes the electrochemical products (R^{2-}) and favorably shifts the electrode potential in the positive direction. Given its low concentration, the dissolved CO_2 is quickly depleted, and thus the binding reaction ceases and the electrode potential transitions to the more negative plateau region. The second stage of the cycle is absorption, which involves mass transfer accompanied by a CO_2 binding reaction. Mass transfer between gaseous CO_2 in the feed gas (e.g., flue gas) and dissolved CO_2 is driven by CO_2 chemical potential differences between the two phases. The simultaneous binding of CO_2 by the capture molecule reduces the dissolved CO_2 concentration, further driving mass transfer from the gas to the liquid. The third stage of the cycle is referred to as anodic deactivation, where the capture molecule is electrochemically oxidized and thus deactivated for CO_2 binding. The first plateau represents the $R(CO_2)^{2-} \rightarrow R(CO_2)^- + e^-$ reaction accompanied by CO_2 release, $R(CO_2)^- \rightarrow R^- + CO_2$, due to the low binding affinity of R^- towards CO_2. Then, the second plateau represents the R^- oxidation reaction, $R^- \rightarrow R + e^-$. Finally, to complete the cycle, the fourth stage is the CO_2 release reaction accompanied by a mass transfer step between the deactivated electrolyte and the CO_2-rich product driven by chemical potential differences between dissolved CO_2 in the deactivated electrolyte and CO_2 in the product gas. The energy required to separate CO_2 in this example case is 24.1 kJ (mol CO_2)$^{-1}$ and can be compared to the minimum work of separation to quantify system energy penalties. Considering $W_{\min}$ for 90% CO_2 removal from a 15 mol% feedstock, which is 6.4 kJ (mol CO_2)$^{-1}$, this translates to an energy penalty of 17.7 kJ (mol CO_2)$^{-1}$ for the cycle in Figure 2. These losses are due to CO_2 chemical potential gradients between the system and the CO_2-containing gases, termed external

irreversibilities. These gradients are necessary to drive finite-rate CO_2 mass transfer from the higher CO_2 concentration feed gas to the lower CO_2 concentration electrolyte during absorption, and from the higher CO_2 concentration electrolyte to the lower CO_2 concentration product gas during desorption.

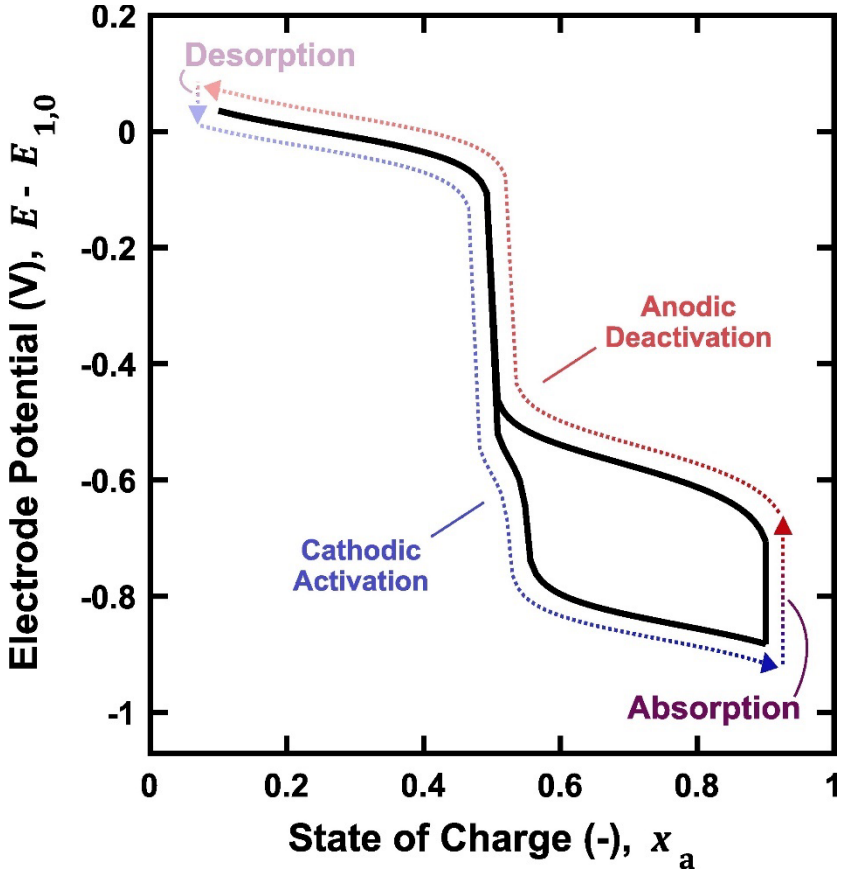

Figure 2. The ideal thermodynamic cycle for a four-stage system for the base case. The black curves represent the electrode potentials. The dotted lines trace the cycle path and stages including cathodic activation, CO_2 absorption from the feed gas, anodic deactivation of the capture species, and CO_2 desorption to the product gas. The following parameter values were used for this example: T = 298.15 K, Δx_a = 0.8, $\tilde{H}_{CO_2}$ = 0.1, r_D = 0.5, $K_{g,1}$ = 10^{-4}, $K_{g,2}$ = 10^{-3}, $K_{g,3}$ = 7.32 × 10^3, and $E_{1,0} - E_{2,0}$ = 0.85 V.

The energy penalties due to external irreversibilities associated with the thermodynamic cycle are dependent upon various material and system properties. Two key parameters are the binding strength of R^{2-} for gas-phase CO_2, $K_{CO_2(g),3}$, and the relative CO_2 solubility, $\widetilde{H}_{CO_2}$. If $K_{CO_2(g),3}$ is varied from 10^0 to 10^{15}, which aligns with reported values of the binding constant ($K_{CO_2,3}$) and Henry's constant for CO_2 (H_{CO_2}),[48,54] the resulting energetic losses span a range of ~100 kJ (mol CO_2)$^{-1}$. When varying $K_{CO_2(g),3}$ from 10^0 to 10^{15} at the intermediate relative CO_2 solubility value considered in the base case ($\widetilde{H}_{CO_2}$ = 0.1), the energy penalty ranged from 0 to 77.2 kJ (mol CO_2)$^{-1}$. Increasing $\widetilde{H}_{CO_2}$ to 0.3 resulted in slightly reduced penalties of 0–68.3 kJ (mol CO_2)$^{-1}$, whereas decreasing $\widetilde{H}_{CO_2}$ to 0.01 yielded slightly greater penalties of 4.2–84.4 kJ (mol CO_2)$^{-1}$, all for the same range of $K_{CO_2(g),3}$ values. When considering the trends of $K_{CO_2(g),3}$, increasing the CO_2 binding strength of the activated species leads to lower CO_2 concentrations in the electrolytes following the activation step. In turn, this increases the chemical potential gradient between the higher CO_2 concentration feed gas and the lower CO_2 concentration electrolyte during absorption. At the largest $K_{CO_2(g),3}$ value of 10^{15}, the energy penalty falls within the range of 68.3–84.4 kJ (mol CO_2)$^{-1}$. These values are significant, approaching the total energy requirements for state-of-the-art thermochemical systems (≥100 kJ (mol CO_2)$^{-1}$).[20–22,22–25] As $\widetilde{H}_{CO_2}$ is decreased from 0.3 to 0.01, the energy penalty may increase by up to ca. 16 kJ (mol CO_2)$^{-1}$, primarily due to the chemical potential gradients in the desorption stage. When $\widetilde{H}_{CO_2}$ is at its lower bound of 0.01, the capture species concentration is much greater than the physical solubility of CO_2 (at atmospheric pressure, P_0). Therefore, as the capture species is deactivated and CO_2 is simultaneously released, the electrolyte is rapidly saturated with CO_2 beyond the solubility limit (i.e., $H_{CO_2}P_0$). This results in a higher chemical potential gradient between the electrolyte containing deactivated capture species

and the CO_2-rich product stream during desorption. Increased values of $\widetilde{H}_{CO_2}$ reduce this chemical potential gradient, and, in turn, lower the energy requirements. Consequently, materials selection plays an important role in determining the system energetic efficiency.

It is important to note that system optimization is not solely dependent on minimization of energy losses. Performance tradeoffs may occur as properties are changed, such as that between the energetic efficiency and the faradaic efficiency (i.e., the moles of CO_2 separated per mole of electron transferred, also referred to as the electron utilization).[32] While lower $K_{CO_2(g),3}$ values increase energetic efficiency, this simultaneously decreases faradaic efficiency. Furthermore, higher $\widetilde{H}_{CO_2}$ values lead to improved energetic efficiency but reduce the faradaic efficiency as the quantity of CO_2 that remains dissolved in solution is higher relative to the amount that is bound/unbound by the capture molecule. The fraction of CO_2 that can be removed from the feed gas is also reduced at decreased $K_{CO_2(g),3}$ and increased $\widetilde{H}_{CO_2}$ values. As such, optimization of material and system properties by balancing performance tradeoffs will require further analyses accounting for process economics that are beyond the scope of this contribution.

3.2 Mass Transport Within the Cell

Next, we evaluate the impact of mass transport on cell performance by varying γ_{mt}, which represents the rate of the electrochemical reaction at the electrode surface (i_n/F) relative to the rate of species mass transport between the electrode surface and bulk solution ($D_R C_{tot}/\delta$). The γ_{mt} parameter can also be thought of as the ratio of the normal current density to the normal limiting current density, $i_n/i_{n,lim}$, where $i_{n,lim} = FD_R C_{tot}/\delta$. To isolate the effect of mass transport, we assume that the homogeneous reactions are at equilibrium, and that electron transfer rates can be described by Nernstian kinetics (i.e., $\gamma_{el} \rightarrow 0$). Figure 3 illustrates the impact of γ_{mt}

on system energetics for the base set of parameters described previously. At low values of γ_{mt} ($\ll$ 1), the mass transport rate is high relative to the electrochemical reaction rate, and species concentrations at the electrode surface are similar to those in the bulk. Therefore, mass transfer resistances across the BL are negligible and the concentration overpotential approaches 0. As γ_{mt} increases, the slowing rates of mass transport (relative to the electrochemical reaction rate) cause the formation of concentration gradients across the BL, increasing overpotentials (i.e., concentration overpotential/polarization). As γ_{mt} approaches 0.2, the system begins to experience mass transport limitations at the ends of cathodic activation and anodic deactivation where reactants become depleted. This can result in marked energy penalties, up to 22.5 and 18.5 kJ (mol CO_2)$^{-1}$ at the cathode and anode, respectively. The penalties from both electrodes can reduce the energetic efficiency by up to 16.6% as compared to the case of thermodynamic equilibrium. Further increasing γ_{mt} beyond 0.2 reduces the accessible state of charge swing ($\Delta x_a < 0.8$) and dramatically increases the energy requirements associated with species mass transport.

From the energetic penalty values shown in Figure 3, it is evident that asymmetries exist between the reduction/activation and oxidation/deactivation stages. This is due to the simultaneous occurrence of the homogeneous CO_2 binding and release reactions with the heterogeneous electrode reactions. The extent of CO_2 binding that occurs during cathodic activation is far less than that of CO_2 release during anodic deactivation because the binding reaction is limited by relatively low concentrations of CO_2 dissolved in the electrolyte (as compared to the concentration of the capture molecule). The greater extent of CO_2 release that occurs during anodic deactivation favorably shifts the potential difference between the observed plateaus, which reduces penalties due to mass transport.[55] In comparison, the observed potential difference between the two main plateaus during cathodic activation is larger, leading to greater energy losses during this stage. The

observed asymmetries are also influenced by the molecular properties including $K_{CO_2(g),1}$, $K_{CO_2(g),2}$, $K_{CO_2(g),3}$, $\widetilde{H}_{CO_2}$, r_D, and $E_{1,0} - E_{2,0}$.

Aside from lowering γ_{mt}, different operating strategies can be employed to help reduce energy penalties from mass transport. Figure S1a explores a case where the state of charge swing is reduced to 40% and the cell is operated asymmetrically such that the state of charge swing is restricted to the range of 50% and 90%. At the highest γ_{mt} value of 0.199, the total energy penalty is reduced from 41.0 kJ (mol CO_2)$^{-1}$ (Figure 3) to 21.4 kJ (mol CO_2)$^{-1}$. Additionally, the quantity of CO_2 captured and released is not significantly impacted (Δx_{CO_2} = 0.7140 for the symmetric case vs. Δx_{CO_2} = 0.7133 for the asymmetric case) because the anionic form of the capture species, R^-, does not significantly bind CO_2 ($K_2 \ll 1$). Thus, this strategy reduces overpotentials associated with the R/R^- transformation and directly cycles between the anionic and dianionic forms of the capture molecule. Mass transport losses can also be diminished by implementing capture molecules with a reduced difference between the standard electrode potentials of the R/R^- and R^-/R^{2-} couples ($\Delta E_0 = E_{1,0} - E_{2,0}$). Figure S1b shows the electrode potential curves when ΔE_0 = 0 V, which decreases the energy penalty to 6.7 kJ (mol CO_2)$^{-1}$. These findings align with prior observations for RFBs with two-electron transfer chemistries and molecular engineering approaches developed in this field may be applicable to electrochemical CO_2 separation.[55] Indeed, for the purposes of electrochemical CO_2 separation, both inter- and intramolecular hydrogen bond donors have been shown to shift the potential of the R^-/R^{2-} more positive, although this has also been shown to result in chemistry-specific variations in the CO_2 binding strength of the capture species.[56,57]

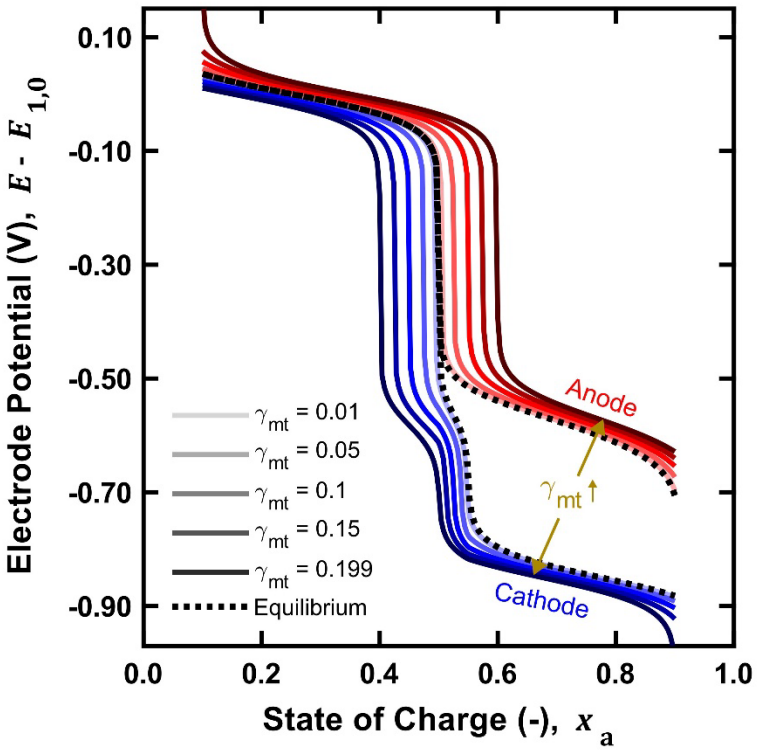

Figure 3. The impact of mass transport on electrode potentials for the base case. γ_{mt} is varied from 0.01 to 0.199, and energy penalties are computed for each electrode by comparing to the equilibrium case (dashed lines, also shown in Figure 2). For each γ_{mt} value, the computed cathode penalties are 1.2, 5.7, 11.1, 16.7, and 22.5 kJ (mol CO_2)$^{-1}$, and the anode penalties are 1.0, 4.7, 9.2, 13.8, and 18.5 kJ (mol CO_2)$^{-1}$. The following parameter values were kept constant for this example: T = 298.15 K, Δx_{a} = 0.8, $\tilde{H}_{\mathrm{CO_2}}$ = 0.1, r_{D} = 0.5, $K_{\mathrm{g},1}$ = 10^{-4}, $K_{\mathrm{g},2}$ = 10^{-3}, $K_{\mathrm{g},3}$ = 7.32 × 10^{3}, and $E_{1,0} - E_{2,0}$ = 0.85 V.

Thus far, we have shown that species mass transport can impact system energy requirements. However, as evident from the definition of γ_{mt}, achievable current densities will also be affected. Electrochemical systems with poor mass transport properties are limited to lower operating current densities, requiring more electrode surface area (and thus more cells) to capture a given quantity of CO_2, which generally results in higher capital costs.[58–61] Typically, when considering system-level performance and costs for electrochemical technologies, the geometric current density is of interest. Given the model assumptions, we can redefine γ_{mt} as a function of the geometric current

density: $\gamma_{\mathrm{mt}} = i_{\mathrm{n}}/i_{\mathrm{n,lim}} \equiv i_{\mathrm{g}}/i_{\mathrm{g,lim}}$. The geometric limiting current density can then be defined as $i_{\mathrm{g,lim}} = a_{\mathrm{v}} k_{\mathrm{m,R}} L_{\mathrm{elec}} F C_{\mathrm{tot}}$, where a_{v} is the electrode area per unit electrode volume ($m^2\ m^{-3}$), $k_{\mathrm{m,R}}$ is the mass transfer coefficient of the capture species ($m\ s^{-1}$), and L_{elec} is the electrode thickness.[62–65] Here, the mass transfer coefficient ($k_{\mathrm{m,R}} \equiv D_{\mathrm{R}}/\delta$) is defined as the mass transport of the capture species through the BL in the absence of homogeneous reactions. In general, this parameter is critical to performance for various technologies that involve mass transfer between a fluid and a solid surface[66,67] and is an empirical value dependent on various fluid properties (e.g., density, viscosity, species diffusivities), surface geometry/properties, and fluid dynamic conditions. While a direct dependence on the species diffusivity (D_j) is apparent from the definition of $k_{\mathrm{m},j}$, all of the properties listed are assumed to impact the BL thickness, δ.[67]

To assess the possible values of $k_{\mathrm{m},j}$ (and thus γ_{mt}), we hypothesize that cell designs for electrochemical CO_2 separation will be similar to contemporary RFB cells, as these formats have been used in recent experimental studies.[14,18,19,35] Prior studies have predicted mass transfer coefficients across a wide range of ca. 5.9×10^{-8} – 6.0×10^{-4} $m\ s^{-1}$ depending on the redox electrolyte composition, cell configuration, and method of analysis.[65,68–71] Given the uncertainties in predicted mass transfer coefficients, it is also common to consider the multiplicative product of a_{v} and $k_{\mathrm{m},j}$, which is referred to as the volumetric mass transfer coefficient, $a_{\mathrm{v}} k_{\mathrm{m},j}$ (s^{-1}). Prior RFB studies have predicted volumetric mass transfer coefficients in the range of ca. 0.1–100 s^{-1} for RFBs.[65,70,72] To avoid the variability associated with reported a_{v} values, we use reported $a_{\mathrm{v}} k_{\mathrm{m},j}$ values rather than $k_{\mathrm{m},j}$ to estimate γ_{mt} values. While we use the aforementioned range of $a_{\mathrm{v}} k_{\mathrm{m},j}$ values for this analysis, we note that these values depend electrolyte properties, electrode/cell properties, and fluid dynamic conditions,[73] all of which remain an open area of research for

electrochemical CO_2 separation. Assuming a capture species concentration of 1 M and an electrode thickness of 500 μm, the lower and upper bound values for $a_v k_{m,R}$ translate to limiting normal current densities of $i_{g,lim}$ = 480 and 4.8 × 10^5 mA cm^{-2}, respectively. For relatively slow mass transport ($k_{m,R}$ = 0.1 s^{-1}) and assuming an 80% state of charge swing (i.e., γ_{mt} < 0.2), the system may be limited to geometric current densities < 96 mA cm^{-2}, slightly below ranges typically cited as desirable in the literature (i.e., $i_g \geq$ 100 mA cm^{-2}).[74–77] When cell and system properties that enable faster mass transport ($a_v k_{m,j}$ = 100 s^{-1}) are adopted, increased geometric current densities may be realizable. Overall, the design or selection of electrodes and electrolytes that enable facile mass transport will be important for achieving target conversion rates (i.e., state of charge swings) with adequate current densities. Other parameters, such as electrolyte flow rates, will also influence electrode mass transfer; therefore, molecular and electrolyte properties must be balanced with operational strategies to achieve optimal performance regimes.

3.3 Heterogeneous Kinetics

Next, we consider the role of heterogeneous kinetics on performance using the γ_{el} parameter, which represents the rate of the electrochemical reaction relative to its intrinsic rate. Figure 4 shows the impact of γ_{el} on the electrode potentials for γ_{el} = 0.01–1. We assess the effect of heterogeneous kinetics in isolation by setting γ_{mt} to a sufficiently low value (γ_{mt} = 10^{-5}). As γ_{el} approaches zero (ca. $\gamma_{el} \leq$ 0.01), energy losses due to electrochemical reaction kinetics become negligible. In contrast, with increasing kinetic limitations represented by γ_{el} values of 0.05, 0.17, 0.5, and 1, total energy losses (summation of the cathodic reduction and anodic oxidation steps) also increase to 7.6, 16.7, 29.62, and 41.2 kJ (mol CO_2)$^{-1}$, respectively. Asymmetries between the cathode and anode overpotentials are again evident, despite imposing equivalent γ_{el} parameters at both

electrodes. In Figure 4, when γ_{el} is set to 1, the energy loss at the cathode is 14.9 kJ (mol CO_2)$^{-1}$, while that at the anode is 26.1 kJ (mol CO_2)$^{-1}$. This difference is due to the disparate concentrations of the capture species in its different forms during the cathodic and anodic processes. Under the assumption of equilibrium homogeneous reactions, this is driven solely by the differences in CO_2 concentrations, which directly impact the relative concentrations of bound and unbound forms of the capture species. Overall, these concentrations alter the exchange current density and therefore the relationship between the current density and activation overpotential (see Equations 24 and 25).

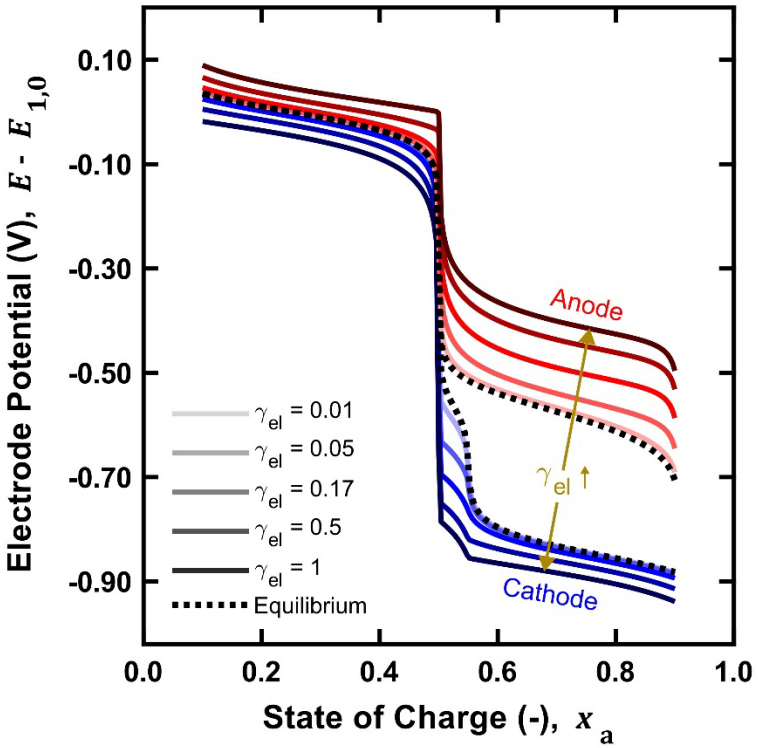

Figure 4. The impact of electrochemical kinetics on electrode potentials investigated by varying γ_{el}. In this case, the effects of mass transfer are negligible (γ_{mt} = 10^{-5}). The penalty for each γ_{el} value is 0.7, 2.1, 4.7, 9.6, and 14.9 kJ (mol CO_2)$^{-1}$ at the cathode and 1.2, 5.2, 11.8, 19.8, and 26.1 kJ (mol CO_2)$^{-1}$ at the anode. For this case, the homogeneous reactions were assumed to be at equilibrium ($Da \to \infty$), and the additional constant parameter values are as follows: T = 298.15 K, Δx_a = 0.8, $\widetilde{H}_{CO_2}$ = 0.1, r_D = 0.5, $K_{g,1}$ = 10^{-4}, $K_{g,2}$ = 10^{-3}, $K_{g,3}$ = 7.32 × 10^3, and $E_{1,0} - E_{2,0}$ = 0.85 V.

These results can be related to experimental molecular and system properties to estimate penalties of present-day chemistries associated with heterogeneous kinetics. Accordingly, we relax the assumption that $\gamma_{\mathrm{mt}} = 10^{-5}$ to represent more practical operating current densities. Figure S2 in the SI demonstrates the impact of varying γ_{el} values when $\gamma_{\mathrm{mt}} = 0.199$. There are slight differences between the penalty values associated with electrochemical kinetics for $\gamma_{\mathrm{mt}} = 0.199$ (Figure S2) and $\gamma_{\mathrm{mt}} = 10^{-5}$ (Figure 4), which is due to coupling effects of the different variables (detailed in Section 3.6). However, the trends of penalties from electrochemical kinetics are similar for different γ_{mt} values; therefore, we use these results to investigate how we expect current chemistries and system designs to compare. To do so, we express γ_{el} as the ratio of γ_{mt} to a new variable, λ (i.e., $\gamma_{\mathrm{el}} = \gamma_{\mathrm{mt}}/\lambda$), which we define as the intrinsic rate of the electrochemical reaction relative to the rate of mass transport ($\lambda = \delta k_0/D_{\mathrm{R}} = k_0/k_{\mathrm{m,R}}$). For the case of symmetrically operating an 80% state of charge swing, where $\gamma_{\mathrm{mt}} < 0.2$, we predict that chemistries and cell designs with $\lambda \geq 20$ (and thus $k_0 \geq 20k_{\mathrm{m,R}}$) will have sufficiently facile heterogeneous kinetics. In Section 3.2, we highlighted that $k_{\mathrm{m},j}$ values are estimated within the range of ca. 5.9×10^{-8} – 6.0×10^{-4} m s^{-1} for RFBs. Further, for organic molecules in aprotic solvents, which is a typical chemistry for direct electrochemical CO_2 separation, heterogeneous (i.e., electrochemical) rate constants (k_0) have been reported in the range of ca. 10^{-3} – 1 cm s^{-1} for relevant redox species (i.e., quinones, phenazine, 2,1,3-benzothiadiazole).[78–83] Considering these parameter value ranges, λ values may be expected to fall within the range of 1.7×10^{-2} to 1.7×10^{4}. At a γ_{mt} of ca. 0.199, this yields a γ_{el} in the range of 1.2×10^{-2} – 12, suggesting that energy losses associated with heterogeneous kinetics may be significant. Accordingly, careful measurement of electrochemical reaction kinetics (as well as cell mass transfer coefficients) will be important for emerging capture

chemistries. While there are several studies that report rate constants for relevant molecules in their unbound states, as cited above, these values may change for the CO_2-bound capture molecules. This will particularly important for the activation overpotential during the anodic deactivation stage, where $R(CO_2)^{2-} \rightarrow R(CO_2)^{-} + e^{-}$ is a dominant reaction.

3.4 Homogeneous Kinetics

Within the four-stage system configuration, external unit operations (e.g., absorption column, degasser) are used to drive CO_2 absorption and release. However, as alluded to earlier, the homogeneous reactions involving CO_2 may also occur within the electrochemical reactor. Due to its finite solubility within the electrolyte, CO_2 is present in the electrochemical cell during cathodic activation. Thus, any R^{2-} formed during this reduction step can bind dissolved CO_2. During anodic deactivation, $R(CO_2)^{-}$ is directly formed from the oxidation reaction and, due to its low affinity for CO_2 in the assumed mechanism, this species can undergo a CO_2 release reaction within the cell. Both homogeneous reactions present in the electrochemical cell shift the relative concentrations of the capture species, and, in turn, impact the electrode potentials. To assess the impact of homogeneous kinetics, Figure 5 compares two bounding cases: (1) equilibrium homogeneous reactions ($Da \rightarrow \infty$) and (2) no homogeneous reactions ($Da \rightarrow 0,\ \omega Da \rightarrow 0$). When the rates of these homogeneous reactions are slow relative to the relevant timescales of the electrochemical reactor (i.e. in the case of $Da \rightarrow 0$), the cell energy requirements increase. The important specific timescales include the PBR reactor residence time (τ) and the diffusion time (δ^2/D_i) for the bulk and BL solutions, respectively. For the example considered here, the total energy penalty of such slow reactions is 22.9 kJ (mol CO_2)$^{-1}$, which would have a relatively significant impact on the system energetic efficiency (ca. 12.9% decrease as compared to the case

of thermodynamic equilibrium). This penalty is a result of how CO_2 binding and release reactions impact the electrode potentials. When these homogeneous reactions occur rapidly ($Da \rightarrow \infty$), the products of the electrochemical reactions are removed, favorably shifting the electrode potentials. When the reactions are infinitely slow ($Da = 0$), this effect is diminished, leading to the observed penalty.

We again observe significant asymmetry between the cathode and anode in Figure 5, which exhibit energetic penalties of 3.8 and 19.1 kJ (mol CO_2)$^{-1}$, respectively, due to a higher possible extent of reaction for CO_2 release at the anode as compared to CO_2 binding at the cathode. Recall that, during cathodic activation, the amount of CO_2 present is limited by the physical solubility of CO_2 in the electrolyte and its concentration is generally much lower than the capture species. Therefore, CO_2 binding is reactant-limited and turning this reaction "off" by assuming slow kinetics does not significantly impact cathode potential. Conversely, anodic deactivation directly produces the only reactant for the CO_2 release ($R(CO_2)^-$); thus, this reaction is not operating under a reactant-limited regime and can occur to a greater extent than CO_2 binding at the cathode. This then results in a greater potential shift at the anode when this reaction has sluggish kinetics.

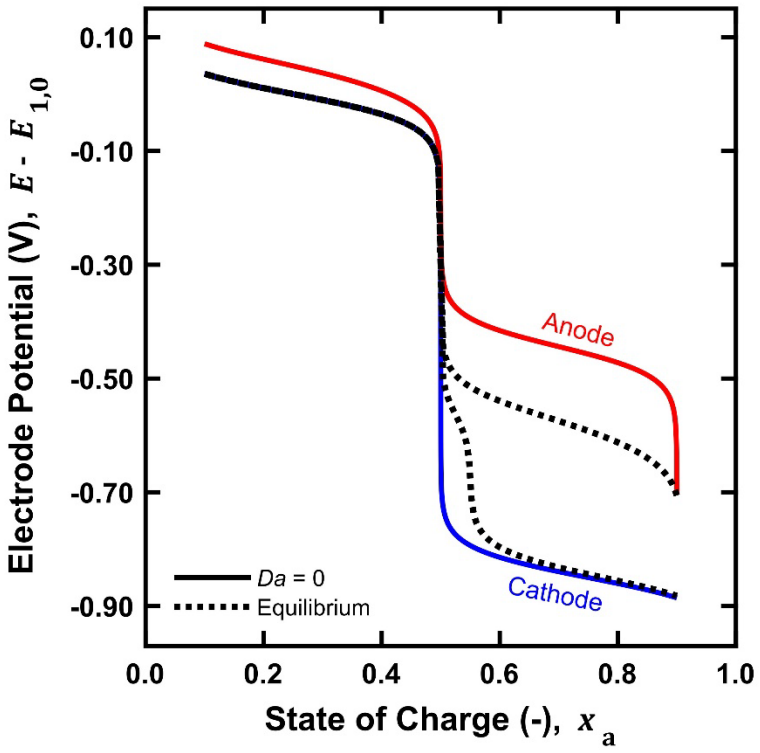

Figure 5. The impact of homogeneous kinetics on electrode potentials by comparing the case of equilibrium kinetics to the case of no homogeneous reactions (Da = 0). In the latter case, the penalty at the cathode and the anode is 3.8 and 19.1 kJ (mol CO_2)$^{-1}$, respectively. The additional constant parameter values are as follows: T = 298.15 K, Δx_a = 0.8, $\tilde{H}_{CO_2}$ = 0.1, r_D = 0.5, $K_{g,1}$ = 10^{-4}, $K_{g,2}$ = 10^{-3}, $K_{g,3}$ = 7.32 × 10^3, and $E_{1,0} - E_{2,0}$ = 0.85 V.

Based on these results, the impact of homogeneous reactions within the electrochemical cell cannot be overlooked when considering the energetic efficiency of a four-stage configuration. Characterizing the kinetic rates of these reactions, especially the rate of CO_2 release, will be important when considering cell energy penalties. However, we note that this analysis does not contemplate the potential for or effect of degasification following CO_2 release. The formation of gas bubbles within a constant-volume anode compartment can lead to increased overpotentials by displacing liquid electrolyte, which decreases ionic conductivity and/or blocks reaction sites.[84,85]

Therefore, while CO_2 release at the anode can remove electrochemical products and favorably shift the potential, if the reaction rate is not properly controlled, bubbles may disrupt system operation.

3.5 Ohmics

To understand the impact of ohmic resistance, we introduce a dimensionless parameter, σ (defined in Table 1), which represents the ratio of the resistance to ionic transport across the membrane/separator to the mass transport resistance within the porous electrode. When $\sigma \ll 1$, the ohmic resistance is relatively small and the associated energy penalty is negligible. Conversely, when $\sigma \gg 1$, the ohmic resistance is dominant and can lead to large energy penalties. In the latter case, the operating current density may be limited by the ohmic resistance (rather than by mass transport) in order to manage cell energy requirements. To quantify the impact of σ, we assume γ_{mt} is at its maximum value of 0.199. For σ values of 0.01, 0.1, 1, 10 and 100, the ohmic overpotential is 0.051, 0.51, 5.1, 51, and 510 mV, respectively. Assuming $\Delta x_{\mathrm{a}} = 0.8$ and $\Delta x_{\mathrm{CO_2}} = 0.714$ (base case conditions), the associated energy penalties are 0.011, 0.11, 1.1, 11, and 110 kJ (mol CO_2)$^{-1}$, respectively.

To estimate expected σ values of present-day material sets and capture chemistries, we again find RFB systems to be a useful analog. An important property to characterize membranes/separators, and used to define σ in this work, is the area-specific resistance, ASR (Ω m^2). For state-of-the-art devices, ASR values are typically in the range of ca. 0.5–20 Ω cm^2.[86–90] To get a lower bound on expected σ values, we assume mass transport is slow ($a_{\mathrm{v}} k_{\mathrm{m,R}} = 0.1$ s^{-1}). With the assumption that $C_{\mathrm{tot}} = 1$ M and $L_{\mathrm{elec}} = 500$ μm, σ ranges from 9–375 and increases further if $a_{\mathrm{v}} k_{\mathrm{m,R}}$ becomes larger. Based on the estimated σ values (9–375), ohmic losses can result in penalties of up to 415 kJ (mol CO_2)$^{-1}$, which can reduce the energetic efficiency by up to 25%

compared to the case of thermodynamic equilibrium. Therefore, the ohmic resistance of the membrane/separator has the potential to be the most significant energy penalty source within the four-stage configuration for electrochemical CO_2 separation systems. These losses can be mitigated through careful selection of component materials, electrolyte formulations, and cell configurations to enable lower σ values and/or by operating at lower current densities (i.e., lower γ_{mt}).

3.6 The Additive Effects of Different Penalty Sources

Next, we focus on the cumulative impact of energetic penalties for these different sources on the PBR electrode models. Note that ohmic losses are not included here as they are an extra additive penalty outside of the PBR electrode models within the developed framework, but are discussed in a subsequent section. We specifically generate electrode potential curves including penalties from all previously described sources to determine the cumulative energy requirements and to explore the interplay between reaction kinetics and mass transport. Then, the penalties associated with each phenomenon are evaluated using an approach similar to voltage-breakdown analyses of polarization curves.[91] Such analyses are important for identifying performance-limiting processes and highlighting opportunities for the greatest improvement. To this point, we have considered each loss in isolation; however, when considering multiple sources at a time, their isolated effects do not directly translate and sum to the overall observed energy requirements. Therefore, to evaluate penalties associated with each mechanism we employ a cumulative limiting case analysis, where one source is removed at a time from the overall polarization curve to quantify its associated contribution.

Figure 6 highlights the cumulative impact of mass transport, homogeneous kinetics, and heterogeneous kinetics at their bounding values of $\gamma_{mt} = 0.199$, $Da = 0$, and $\gamma_{el} = 1$, in addition to the thermodynamic cycle. The total energy required for this example case is 111.3 kJ (mol CO_2)$^{-1}$. The dark red and blue curves represent the anode and cathode potential traces, respectively. Each of the red and blue shaded regions represents energetic penalties resulting from resistive losses associated with mass transport, homogeneous kinetics, and heterogeneous kinetics. The gray shaded region indicates the work of the internally reversible thermodynamic cycle (i.e., has external irreversibilities) for this four-stage system. For this analysis, the impact of mass transport was evaluated first by taking the difference between the total energy requirements and the value when the impact of mass transport is removed (i.e., $\gamma_{mt} = 5\times10^{-5}$, while Da and γ_{el} are held constant at 0 and 1, respectively). The computed penalty associated with mass transport is 24.2 kJ (mol CO_2)$^{-1}$ for the cathode and 14.8 kJ (mol CO_2)$^{-1}$ for the anode. Subsequently, the penalties from homogeneous kinetics were assessed by calculating the difference between the case where only the mass transport impact was removed ($\gamma_{mt} = 5\times10^{-5}$, $Da = 0$, and $\gamma_{el} = 1$) to a case where both the mass transport and homogeneous kinetics impacts are removed ($\gamma_{mt} = 5\times10^{-5}$, $Da \rightarrow \infty$, and $\gamma_{el} = 1$). The cathode and anode penalties associated with homogeneous kinetics in this case are 0.6 and 6.6 kJ (mol CO_2)$^{-1}$, respectively. The penalties associated with heterogeneous kinetics were then evaluated by calculating the difference between the case of isolated heterogeneous kinetics ($\gamma_{mt} = 5\times10^{-5}$, $Da \rightarrow \infty$, and $\gamma_{el} = 1$) and the thermodynamic cycle potentials. These values are equivalent to those from Figure 4, which are 14.9 kJ (mol CO_2)$^{-1}$ and 26.1 kJ (mol CO_2)$^{-1}$ for the cathode and anode, respectively. Finally, the energy required for the reversible thermodynamic cycle was determined to be 24.2 kJ (mol CO_2)$^{-1}$ and the energy penalty associated with the external

irreversibilities of the system was calculated to be 17.8 kJ (mol CO_2)$^{-1}$ by comparing to the minimum work of capturing 90% of the CO_2 from a 15% CO_2 feed gas composition.

From this breakdown, we note that the penalties from mass transport and homogeneous kinetics evaluated in Figure 6 are distinct from those shown in Figures 3 and 5, when their effects were explored in isolation. Specifically, a coupling effect exists between concentration changes due to homogeneous kinetics and the bulk equilibrium potential, concentration overpotential, and activation overpotential for each electrochemical reaction. First considering the mass transport impact, operating at a high γ_{mt} value of 0.199 depletes the electrochemical reactants near the electrode surface and enriches the nearby electrolyte solution with the products. These concentrations directly impact the exchange current density (see, Equation 25), and therefore the activation overpotential (see, Equation 24). Then considering the effect of homogeneous kinetics, eliminating homogeneous reactions alters the concentration profiles throughout the electrodes, which also impacts the exchange current density (see, Equations 24 and 25). Concentration changes associated with homogeneous kinetics can also impact observed concentration overpotentials. Due to these interconnectivities, energy penalties associated with each phenomenon are dependent upon the order in which they are evaluated. To demonstrate this, Figure S3 in the SI switches the order of heterogeneous kinetics and homogeneous kinetics, such that the heterogeneous kinetics mechanism is removed before homogeneous kinetics. Under this scenario, the penalty attributed to heterogeneous kinetics is smaller than that in Figure 6, whereas the penalty from homogeneous kinetics is larger. Accordingly, caution is required when utilizing loss breakdown techniques, since the order in which each effect is removed matters. Nonetheless, if a consistent order is used, breakdown methods can be helpful for estimating the relative impact of each individual penalty source on the overall, cumulative energy requirements. At the base case

conditions used here, it is apparent that all penalty sources make non-negligible contribution and must be considered when contemplating the energetics of electrochemical CO_2 separation systems.

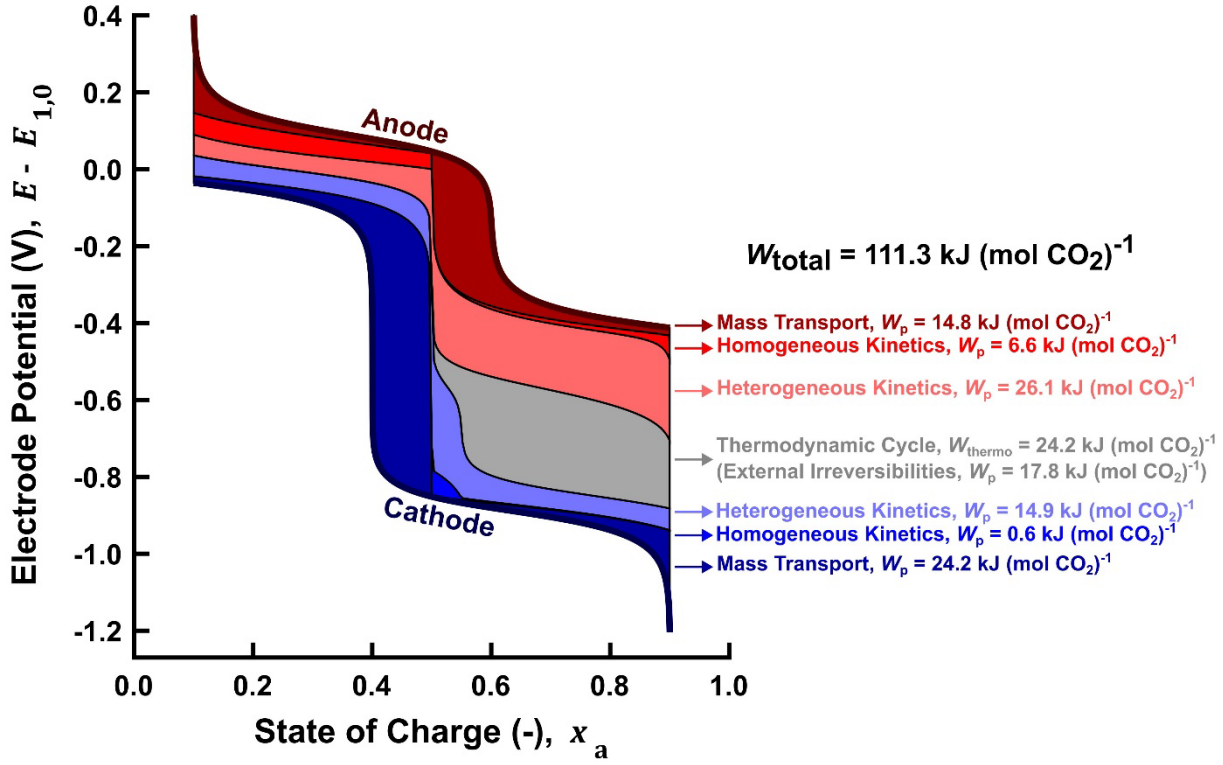

Figure 6. The combined effect of mass transport (γ_{mt} = 0.199), homogeneous kinetics (Da = 0), and heterogeneous kinetics (γ_{el} = 1), on top of the thermodynamic cycle (which includes external irreversibilities). The figure quantifies the energetic penalty, W_p (kJ (mol CO_2)$^{-1}$), of each source and demonstrates how these penalties contribute to the overall, cumulative energy requirements of 111.3 kJ (mol CO_2)$^{-1}$. The minimum work is considered for a case of 90% CO_2 capture from a 15% CO_2 feed gas source (W_{min} = 6.4 kJ (mol CO_2)$^{-1}$), which is used to compute the penalty from external irreversibilities. Additionally, other constant parameter values are as follows: T = 298.15 K, Δx_a = 0.8, $\tilde{H}_{CO_2}$ = 0.1, r_D = 0.5, $K_{g,1}$ = 10^{-4}, $K_{g,2}$ = 10^{-3}, $K_{g,3}$ = 7.32 × 10^3, and $E_{1,0} - E_{2,0}$ = 0.85 V.

3.7 Exploring Pathways to Reduce System Energy Requirements

Building on the previous section, the model can also be used to explore different energy reduction pathways through material innovations, reactor engineering, and/or modifying operating conditions. As we now consider the full cell, penalties from ohmics are considered along with

mass transport, homogeneous kinetics, heterogeneous kinetics, and external irreversibilities. We note that the individual energy penalty from each mechanism within the electrodes (i.e., mass transport, homogeneous kinetics, and heterogeneous kinetics) was determined using the approach described in Section 3.6, Then the ohmic overpotential was added on as an additional penalty. To demonstrate this utility, we show an example pathway for lowering energy requirements in Figure 7. Here, we again consider 90% capture of CO_2 from a feed gas containing 15% CO_2. For the initial case, we consider a capture chemistry with a standard potential difference, ΔE_0 or $E_{1,0} - E_{2,0}$, of 0.85 V, the base case of our previous calculations. We assume that the electrochemical reactor is operated at its maximum current density (γ_{mt} = 0.199), both heterogeneous and homogeneous kinetics are slow (i.e., λ = 0.199, Da = 0), and the ohmic resistance is moderately high (σ = 50). All other assumed parameter values are listed in the caption of Figure 7. Under these conditions, the energy required for separation is 167 kJ (mol CO_2)$^{-1}$; however, through a series of system improvements, this can be lowered to 54 kJ (mol CO_2)$^{-1}$. In the first incremental improvement, we contemplate a scenario where a capture chemistry with a reduced standard potential difference of 0.5 V between the R/R^- and R^-/R^{2-} couples is selected, resulting in a 20 kJ (mol CO_2)$^{-1}$ diminution. As described in Section 3.2, this reduces mass transport penalties due to decreased concentration overpotentials. In the second improvement, γ_{mt} is reduced to 0.1, which is approximately half of its initial value, resulting in a 39 kJ (mol CO_2)$^{-1}$ decrease. Independently decreasing γ_{mt}, as such, can be thought of as lowering the operating current density of the electrochemical reactor. As such, all resistive contributions are reduced; however, in a process design scenario, this would need to be balanced with increased cell area and capital costs. The third improvement considers faster kinetics for both heterogeneous (λ = 2) and homogeneous ($Da \rightarrow \infty$) reactions. Based on these parameter values, the penalty for electrochemical kinetics is

significantly reduced, and that associated with the homogeneous reactions is eliminated. This leads to a 40 kJ (mol CO_2)$^{-1}$ decrease in the energy requirements. Finally, the fourth improvement sees a decrease in the ohmic resistance of the cell to from $\sigma = 50$ to $\sigma = 25$, in line with current estimated values (see Section 3.5). In practice, reducing σ could be realized by using a thinner and/or more conductive membrane/separator. This results in a 14 kJ (mol CO_2)$^{-1}$ reduction, lowering the total energy requirements to 54 kJ (mol CO_2)$^{-1}$. We note that this is but one example of how the model can be used to explore different routes to lowering energy requirements, and the pathway shown is not necessarily optimal. Indeed, other pathways can be considered as the feasibility of changing the variables defined in this model may depend on chemistry, reactor design, or application needs.

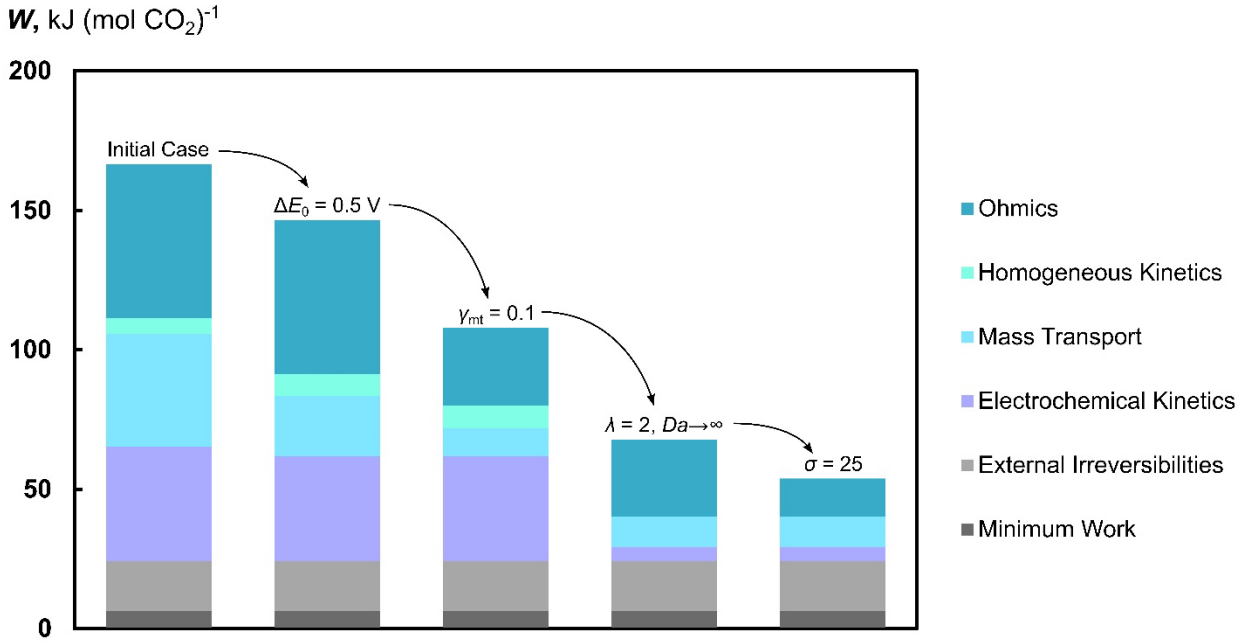

Figure 7. An example use of the electrochemical reactor model for exploring pathways to reduce energy requirements. The bar graph shows the cumulative effective of minimum work, external irreversibilities, electrochemical kinetics, mass transport, homogeneous kinetics, and ohmics on the total energy requirements for five different cases. The initial case assumes the following parameter values: $\Delta E_0 = 0.85$ V, $\gamma_{mt} = 0.199$, $\lambda = 0.199$, $Da = 0$, and $\kappa = 50$. For all cases, the minimum work is considered assuming 90% CO_2 capture from a 15% CO_2 feed gas source (W_{min}

= 6.4 kJ (mol CO_2)$^{-1}$). For all cases, the additional constant parameter values are as follows: T = 298.15 K, $\Delta x_a = 0.8$, $\widetilde{H}_{CO_2} = 0.1$, $r_D = 0.5$, $K_{g,1} = 10^{-4}$, $K_{g,2} = 10^{-3}$, and $K_{g,3} = 7.32\times10^{3}$.

4. CONCLUSIONS

In this study, we presented a dimensionless electrochemical reactor model to predict the cell energy requirements for electrochemically-mediated CO_2 separations. In developing the model, we specifically considered a four-stage system configuration with soluble, redox-active capture molecules (i.e., direct capture method), a post-combustion capture application, where 90% of CO_2 is removed from a 15% feedstock, and a baseline set of conditions informed by current literature. We derived a set of key dimensionless groups to explore the impact of different sources of energetic penalties, including mass transport, heterogeneous kinetics, homogeneous kinetics, and ohmics. We first revisited thermodynamic modeling to establish an upper performance bound for a given system. We specifically modeled the ideal thermodynamic cycle of a four-stage system, and compute the work by accounting for the minimum work of separation and losses due to external irreversibilities. Then, we systematically investigated the impact of mass transport, heterogeneous kinetics, homogeneous kinetics, and ohmics by varying their corresponding dimensionless parameters across a range of values. We use material properties harvested from experimental literature on electrochemical CO_2 separators as well as adjacent electrochemical technologies (e.g., RFBs) to estimate where current chemistries and cell designs may fall within these parameter ranges. Finally, we investigated the cumulative effects of various sources of irreversibility on the total cell energy requirements and highlighted how the model could be used to identify energy reduction pathways. Collectively, this work (1) offers an understanding of why a wide range of energy requirements appears in the published literature, (2) clarifies how different resistive losses contribute to system energetics and the interplay between the underlying

phenomena, and (3) highlights pathways and key variables for improving performance. Finally, while this model was developed for a specific system configuration and capture scenario, we anticipate that this analytical approach can be generalized to other approaches potentially enabling better comparisons across the ever-growing field. Some areas of interest include the evaluation of distinct reaction chemistries, the refinement of reactor configurations, and the consideration of different CO_2 capture applications.

ASSOCIATED CONTENT

The Supporting Information is available and free of charge.

Full list of dimensional governing equations (Section S1); Description of deriving the dimensionless governing equations (Section S2); Description of the two simplifying cases ($Da \rightarrow \infty$ and $Da = 0$) and mathematical manipulations to solve them (Section S3); A section containing supplementary figures discussed throughout the main text (Section S4).

AUTHOR INFORMATION

Corresponding Authors

- **Fikile R. Brushett** – *Department of Chemical Engineering, Massachusetts Institute of Technology, Cambridge, Massachusetts 02139, United Stated;* orcid.org/0000-0002-7361-6637; Email: brushett@mit.edu

Authors

- **Lauren E. Clarke** – *Department of Chemical Engineering, Massachusetts Institute of Technology, Cambridge, Massachusetts 02139, United Stated;* orcid.org/0000-0003-4780-2791; Email: lclarke@mit.edu

Author Contributions

LEC: Conceptualization, Methodology, Validation, Formal analysis, Investigation, Data curation, Writing - original draft, Writing - review & editing, Visualization. **FRB:** Conceptualization, Resources, Writing - original draft, Writing - review & editing, Supervision, Funding acquisition.

Notes

The authors declare no competing financial interest.

ACKNOWLEDGMENTS

The authors gratefully acknowledge funding support from the Exxon Mobil Corporation and thank Corey Kaminsky, Heather Elsen, Bennett Marshall, and Kevin Stevens for their support and insightful discussions. We also gratefully acknowledge funding support from the Alfred P. Sloan Foundation. LEC acknowledges financial support from the MIT MathWorks Engineering Fellowship and the MIT Charles M. Vest Fellowship. Finally, we thank Katelyn Ripley of the Brushett Group for many fruitful discussions on this work.

NOMENCLATURE

Latin Variables and Symbols

a_{v}	Total electrode surface area per electrode volume (m^{-1})
$A_{\mathrm{g,elec}}$	Geometric electrode of the electrode (m^2)
ASR	Area specific resistance ($\Omega\ m^2$)
C_0	Standard concentration (1000 mol m^{-3})
C_i	Concentration of species i (mol m^{-3})
$C_{\mathrm{R,tot}}$	Total capture species concentration (mol m^{-3})
Da	Damköhler number (-)
D_i	Diffusivity of species i ($m^2\ s^{-1}$)
f_i^*	Molar flux of species i exiting the bulk solution and entering the BL solution (mol $m^{-2}\ s^{-1}$)

E	Electrode potential (V vs an arbitrary reference electrode)
$E_{0,k}$	Standard reduction potential of reaction k (V vs an arbitrary reference electrode)
F	Faraday constant (96,485 C mol^{-1})
H_{CO_2}	Henry's law constant for CO_2 (mol m^{-3} Pa^{-1})
$\widetilde{H}_{CO_2}$	Relative CO_2 Solubility, i.e., solubility of CO_2 at 101,325 Pa partial pressure relative to maximum binding capacity, which is C_{tot} (-)
i_0	Exchange current density (A m^{-2})
i_g	Geometric current density (A m^{-2})
i_n	Local, surface-normal current density (A m^{-2})
$i_{n,1}$	Portion of local, surface-normal current density going towards electrochemical reaction 1, the R/R^- couple (A m^{-2})
$i_{n,2}$	Portion of local, surface-normal current density going towards electrochemical reaction 2, the R^-/R^{2-} couple (A m^{-2})
$i_{n,3}$	Portion of local, surface-normal current density going towards electrochemical reaction 3, the $R(CO_2)/R(CO_2)^-$ couple (A m^{-2})
$i_{n,4}$	Portion of local, surface-normal current density going towards electrochemical reaction 4, the $R(CO_2)^-/R(CO_2)^{2-}$ couple (A m^{-2})
k_0	Heterogeneous rate constant (m s^{-1})
k_{bind}	Forward rate constant for CO_2 binding (m^3 mol^{-1} s^{-1})
k_{rel}	Reverse rate constant for CO_2 binding, i.e., CO_2 release rate constant (s^{-1})
k_{comp}	Forward rate constant for comproportionation (m^3 mol^{-1} s^{-1})
k_{disp}	Reverse rate constant for comproportionation, i.e., disproportionation (m^3 mol^{-1} s^{-1})
$K_{CO_2,1}$	Equilibrium constant for binding between dissolved CO_2 and R (-)
$K_{CO_2,2}$	Equilibrium constant for binding between dissolved CO_2 and R^- (-)
$K_{CO_2,3}$	Equilibrium constant for binding between dissolved CO_2 and R^{2-} (-)
$K_{CO_2(g),1}$	Equilibrium constant for binding between gas-phase CO_2 and R (-)

$K_{\mathrm{CO_2(g),2}}$	Equilibrium constant for binding between gas-phase CO_2 and R^- (-)
$K_{\mathrm{CO_2(g),3}}$	Equilibrium constant for binding between gas-phase CO_2 and R^{2-} (-)
$K_{\mathrm{comp,1}}$	Equilibrium constant for comproportionation with R and R^{2-} (-)
$K_{\mathrm{comp,2}}$	Equilibrium constant for comproportionation with $R(CO_2)$ and $R(CO_2)^{2-}$ (-)
$K_{\mathrm{comp,3}}$	Equilibrium constant for comproportionation with R and $R(CO_2)^{2-}$ (-)
$K_{\mathrm{comp,4}}$	Equilibrium constant for comproportionation with $R(CO_2)$ and R^{2-} (-)
L_{elec}	Electrode thickness (m)
n	Number of electrons transferred in a given electrochemical reaction (-)
P_0	Ambient pressure (101,325 Pa)
$P_{\mathrm{CO_2}}$	Partial pressure of CO_2 (Pa)
r_j^{h}	Rate of homogeneous reaction j (mol m^{-3} s^{-1})
$r_{\mathrm{b,1}}^{\mathrm{h}}$	Rate of the homogeneous binding reaction between R and CO_2 (mol m^{-3} s^{-1})
$r_{\mathrm{b,2}}^{\mathrm{h}}$	Rate of the homogeneous binding reaction between R^- and CO_2 (mol m^{-3} s^{-1})
$r_{\mathrm{b,3}}^{\mathrm{h}}$	Rate of the homogeneous binding reaction between R^{2-} and CO_2 (mol m^{-3} s^{-1})
$r_{\mathrm{c,1}}^{\mathrm{h}}$	Rate of the homogeneous comproportionation reaction between R and R^{2-} (mol m^{-3} s^{-1})
$r_{\mathrm{c,2}}^{\mathrm{h}}$	Rate of the homogeneous comproportionation reaction between $R(CO_2)$ and $R(CO_2)^{2-}$ (mol m^{-3} s^{-1})
$r_{\mathrm{c,3}}^{\mathrm{h}}$	Rate of the homogeneous comproportionation reaction between R and $R(CO_2)^{2-}$ (mol m^{-3} s^{-1})
$r_{\mathrm{c,4}}^{\mathrm{h}}$	Rate of the homogeneous comproportionation reaction between $R(CO_2)$ and R^{2-} (mol m^{-3} s^{-1})
r_{D}	Diffusivity ratio of the capture species to CO_2 (-)
r_k^{e}	Rate of electrochemical reaction k (mol m^{-2} s^{-1})
R_{u}	Ideal gas constant (8.314 J mol^{-1} K^{-1})
$s_{i,j}$	Stoichiometric coefficient of species i in homogeneous reaction j (-)
$s_{i,k}$	Stoichiometric coefficient of species i in electrochemical reaction k (-)

T	Temperature (K)
u_{p}	Electrolyte velocity through electrode pores (m s^{-1})
V	Cell voltage (V)
V_{elec}	Electrode volume (m^3)
W	Work (kJ (mol CO_2)$^{-1}$)
W_{min}	Minimum work (kJ (mol CO_2)$^{-1}$)
x_{a}	State of charge (-)
Δx_{a}	State of charge swing (-)
$x_{\mathrm{CO_2}}$	Normalized quantity of total CO_2 in solution (-)
y	Length dimension of the boundary layer (m)
z	Length dimension of the PBR electrode reactors (m)

Greek Variables and Symbols

α_{a}	Anodic charge transfer coefficient (-)
α_{c}	Cathodic charge transfer coefficient (-)
γ_{el}	Dimensionless parameter representing the ratio of the electrochemical reaction rate to the intrinsic electrochemical reaction rate (-)
γ_{mt}	Dimensionless parameter representing the ratio of the electrochemical reaction rate to the mass transport rate in the boundary layer (-)
δ	Boundary layer thickness (m)
η	Overpotential (V)
λ	Dimensionless parameter representing the ratio of the intrinsic electrochemical reaction rate to the mass transport rate in the boundary layer (-)
σ	Dimensionless parameter representing the ratio of the ohmic resistance to the boundary layer mass transport resistance (-)
τ	Residence time of the PBR electrode (s)
ω	Dimensionless parameter representing the ratio of the reactor residence time to the boundary layer mass transport time scale (-)

Subscripts and Superscripts

∞	Bulk electrode pore solution
$*$	Boundary layer solution
act	Activation
an	Anode
cath	Cathode
conc	Concentration
eq	Equilibrium
feed	Feed gas mixture
in	Inlet
ohm	Ohmic
out	Outlet
ox	Oxidized species in the electrochemical reaction
red	Reduced species in the electrochemical reaction
s	Electrolyte solution directly adjacent to the solid electrode surface

Accents

$\sim$	Denotes a dimensionless variable

REFERENCES

(1) *Net Zero by 2050*; IEA: Paris, 2021. https://www.iea.org/reports/net-zero-by-2050 (accessed 2023-07-24).

(2) *CCUS in Clean Energy Transitions*; IEA: Paris, 2020. https://www.iea.org/reports/ccus-in-clean-energy-transitions (accessed 2023-07-24).

(3) *Tracking Carbon Capture, Utilisation and Storage*. IEA. https://www.iea.org/energy-system/carbon-capture-utilisation-and-storage#tracking (accessed 2023-07-24).

(4) *CO_2 Emissions in 2022*; IEA: Paris, 2023. https://www.iea.org/reports/co2-emissions-in-2022 (accessed 2023-07-24).

(5) *An updated roadmap to Net Zero Emissions by 2050*. IEA. https://www.iea.org/reports/world-energy-outlook-2022/an-updated-roadmap-to-net-zero-emissions-by-2050 (accessed 2024-02-16).

(6) Dubey, A.; Arora, A. Advancements in Carbon Capture Technologies: A Review. *J. Clean. Prod.* **2022**, *373*, 133932. https://doi.org/10.1016/j.jclepro.2022.133932.

(7) Dziejarski, B.; Krzyżyńska, R.; Andersson, K. Current Status of Carbon Capture, Utilization, and Storage Technologies in the Global Economy: A Survey of Technical Assessment. *Fuel* **2023**, *342*, 127776. https://doi.org/10.1016/j.fuel.2023.127776.

(8) Socolow, R.; Desmond, M.; Aines, R.; Blackstock, J.; Bolland, O.; Kaarsberg, T.; Lewis, N.; Mazzotti, M.; Pfeffer, A.; Sawyer, K.; Siirola, J.; Smit, B.; Wilcox, J. *Direct Air Capture of CO_2 with Chemicals. A Technology Assessment for the APS Panel on Public Affairs*; American Physical Society, 2011. https://www.aps.org/policy/reports/assessments/upload/dac2011.pdf (accessed 2023-09-25).

(9) Lackner, K. S. The Thermodynamics of Direct Air Capture of Carbon Dioxide. *Energy* **2013**, *50*, 38–46. https://doi.org/10.1016/j.energy.2012.09.012.

(10) Fasihi, M.; Efimova, O.; Breyer, C. Techno-Economic Assessment of CO_2 Direct Air Capture Plants. *J. Clean. Prod.* **2019**, *224*, 957–980. https://doi.org/10.1016/j.jclepro.2019.03.086.

(11) Mutch, G. A. Electrochemical Separation Processes for Future Societal Challenges. *Cell Rep. Phys. Sci.* **2022**, *3* (4), 100844. https://doi.org/10.1016/j.xcrp.2022.100844.

(12) Renfrew, S. E.; Starr, D. E.; Strasser, P. Electrochemical Approaches toward CO_2 Capture and Concentration. *ACS Catal.* **2020**, *10* (21), 13058–13074. https://doi.org/10.1021/acscatal.0c03639.

(13) Diederichsen, K. M.; Sharifian, R.; Kang, J. S.; Liu, Y.; Kim, S.; Gallant, B. M.; Vermaas, D.; Hatton, T. A. Electrochemical Methods for Carbon Dioxide Separations. *Nat. Rev. Methods Primer* **2022**, *2* (1), 1–20. https://doi.org/10.1038/s43586-022-00148-0.

(14) Diederichsen, K. M.; Liu, Y.; Ozbek, N.; Seo, H.; Hatton, T. A. Toward Solvent-Free Continuous-Flow Electrochemically Mediated Carbon Capture with High-Concentration Liquid Quinone Chemistry. *Joule* **2022**, *6* (1), 221–239. https://doi.org/10.1016/j.joule.2021.12.001.

(15) Voskian, S.; Hatton, T. A. Faradaic Electro-Swing Reactive Adsorption for CO_2 Capture. *Energy Environ. Sci.* **2019**, *12* (12), 3530–3547. https://doi.org/10.1039/C9EE02412C.

(16) Liu, Y.; Ye, H.-Z.; Diederichsen, K. M.; Van Voorhis, T.; Hatton, T. A. Electrochemically Mediated Carbon Dioxide Separation with Quinone Chemistry in Salt-Concentrated Aqueous Media. *Nat. Commun.* **2020**, *11* (1), 2278. https://doi.org/10.1038/s41467-020-16150-7.

(17) Diederichsen, K. M.; DeWitt, S. J. A.; Hatton, T. A. Electrochemically Facilitated Transport of CO_2 between Gas Diffusion Electrodes in Flat and Hollow Fiber Geometries. *ACS EST Eng.* **2023**, *3* (7), 1001–1012. https://doi.org/10.1021/acsestengg.3c00030.

(18) Jin, S.; Wu, M.; Jing, Y.; Gordon, R. G.; Aziz, M. J. Low Energy Carbon Capture via Electrochemically Induced pH Swing with Electrochemical Rebalancing. *Nat. Commun.* **2022**, *13* (1), 2140. https://doi.org/10.1038/s41467-022-29791-7.

(19) Rahimi, M.; Catalini, G.; Puccini, M.; Hatton, T. A. Bench-Scale Demonstration of CO_2 Capture with an Electrochemically Driven Proton Concentration Process. *RSC Adv.* **2020**, *10* (29), 16832–16843. https://doi.org/10.1039/D0RA02450C.

(20) Bui, M.; Adjiman, C. S.; Bardow, A.; Anthony, E. J.; Boston, A.; Brown, S.; Fennell, P. S.; Fuss, S.; Galindo, A.; Hackett, L. A.; Hallett, J. P.; Herzog, H. J.; Jackson, G.; Kemper, J.; Krevor, S.; Maitland, G. C.; Matuszewski, M.; Metcalfe, I. S.; Petit, C.; Puxty, G.; Reimer, J.; Reiner, D. M.; Rubin, E. S.; Scott, S. A.; Shah, N.; Smit, B.; Trusler, J. P. M.; Webley, P.; Wilcox, J.; Mac Dowell, N. Carbon Capture and Storage (CCS): The Way Forward. *Energy Environ. Sci.* **2018**, *11* (5), 1062–1176. https://doi.org/10.1039/C7EE02342A.

(21) Chapel, D. G.; Ernest, J.; Mariz, C. L. Recovery of CO_2 from Flue Gases: Commercial Trends. In *Canadian Society of Chemical Engineers annual meeting*; Saskatoon, Saskatchewan Canada, 1999.

(22) Abu-Zahra, M. R. M.; Schneiders, L. H. J.; Niederer, J. P. M.; Feron, P. H. M.; Versteeg, G. F. CO_2 Capture from Power Plants. *Int. J. Greenh. Gas Control* **2007**, *1* (1), 37–46. https://doi.org/10.1016/S1750-5836(06)00007-7.

(23) Miraza, N.; Kearns, D. *State of the Art: CCS Technologies 2022*; Global CCS Institute, 2022. https://www.globalccsinstitute.com/wp-content/uploads/2022/05/State-of-the-Art-CCS-Technologies-2022.pdf (accessed 2024-02-18).

(24) Zhao, B.; Liu, F.; Cui, Z.; Liu, C.; Yue, H.; Tang, S.; Liu, Y.; Lu, H.; Liang, B. Enhancing the Energetic Efficiency of MDEA/PZ-Based CO_2 Capture Technology for a 650MW Power Plant: Process Improvement. *Appl. Energy* **2017**, *185*, 362–375. https://doi.org/10.1016/j.apenergy.2016.11.009.

(25) Karimi, M.; Hillestad, M.; Svendsen, H. F. Capital Costs and Energy Considerations of Different Alternative Stripper Configurations for Post Combustion CO_2 Capture. *Chem. Eng. Res. Des.* **2011**, *89* (8), 1229–1236. https://doi.org/10.1016/j.cherd.2011.03.005.

(26) Kumar Chakrabarti, B.; Kalamaras, E.; Kumar Singh, A.; Bertei, A.; Rubio-Garcia, J.; Yufit, V.; M. Tenny, K.; Wu, B.; Tariq, F.; S. Hajimolana, Y.; P. Brandon, N.; Low, C. T. J.; L. Roberts, E. P.; Chiang, Y.-M.; R. Brushett, F. Modelling of Redox Flow Battery Electrode Processes at a Range of Length Scales: A Review. *Sustain. Energy Fuels* **2020**, *4* (11), 5433–5468. https://doi.org/10.1039/D0SE00667J.

(27) Abdol Rahim, A. H.; Tijani, A. S.; Kamarudin, S. K.; Hanapi, S. An Overview of Polymer Electrolyte Membrane Electrolyzer for Hydrogen Production: Modeling and Mass Transport. *J. Power Sources* **2016**, *309*, 56–65. https://doi.org/10.1016/j.jpowsour.2016.01.012.

(28) Ramadesigan, V.; Northrop, P. W. C.; De, S.; Santhanagopalan, S.; Braatz, R. D.; Subramanian, V. R. Modeling and Simulation of Lithium-Ion Batteries from a Systems Engineering Perspective. *J. Electrochem. Soc.* **2012**, *159* (3), R31. https://doi.org/10.1149/2.018203jes.

(29) Falcão, D. S.; Pinto, A. M. F. R. A Review on PEM Electrolyzer Modelling: Guidelines for Beginners. *J. Clean. Prod.* **2020**, *261*, 121184. https://doi.org/10.1016/j.jclepro.2020.121184.

(30) Catañeda, L. F.; Rivera, F. F.; Pérez, T.; Nava, J. L. Mathematical Modeling and Simulation of the Reaction Environment in Electrochemical Reactors. *Curr. Opin. Electrochem.* **2019**, *16*, 75–82. https://doi.org/10.1016/j.coelec.2019.04.025.

(31) Sanpasertparnich, T.; Idem, R.; Bolea, I.; deMontigny, D.; Tontiwachwuthikul, P. Integration of Post-Combustion Capture and Storage into a Pulverized Coal-Fired Power Plant. *Int. J. Greenh. Gas Control* **2010**, *4* (3), 499–510. https://doi.org/10.1016/j.ijggc.2009.12.005.

(32) Clarke, L. E.; Leonard, M. E.; Hatton, T. A.; Brushett, F. R. Thermodynamic Modeling of CO_2 Separation Systems with Soluble, Redox-Active Capture Species. *Ind. Eng. Chem. Res.* **2022**, *61* (29), 10531–10546. https://doi.org/10.1021/acs.iecr.1c04185.

(33) Hasan, M. M. F.; Baliban, R. C.; Elia, J. A.; Floudas, C. A. Modeling, Simulation, and Optimization of Postcombustion CO_2 Capture for Variable Feed Concentration and Flow Rate. 2. Pressure Swing Adsorption and Vacuum Swing Adsorption Processes. *Ind. Eng. Chem. Res.* **2012**, *51* (48), 15665–15682. https://doi.org/10.1021/ie301572n.

(34) Shaw, R. A.; Hatton, T. A. Electrochemical CO_2 Capture Thermodynamics. *Int. J. Greenh. Gas Control* **2020**, *95*, 102878. https://doi.org/10.1016/j.ijggc.2019.102878.

(35) Jin, S.; Wu, M.; Gordon, R. G.; Aziz, M. J.; Kwabi, D. G. pH Swing Cycle for CO_2 Capture Electrochemically Driven through Proton-Coupled Electron Transfer. *Energy Environ. Sci.* **2020**, *13* (10), 3706–3722. https://doi.org/10.1039/D0EE01834A.

(36) Ali, F.; Modak, S.; Kwabi, D. G. Assessing the Performance Limits of Electrochemical CO_2 Separation Using Exergy Loss Analysis and Zero-Dimensional Modeling. *ACS Sustain. Chem. Eng.* **2023**, *11* (48), 16995–17005. https://doi.org/10.1021/acssuschemeng.3c04867.

(37) Li, S.; Deng, S.; Zhao, L.; Zhao, R.; Yuan, X. Thermodynamic Carbon Pump 2.0: Elucidating Energy Efficiency through the Thermodynamic Cycle. *Energy* **2021**, *215*, 119155. https://doi.org/10.1016/j.energy.2020.119155.

(38) Boualavong, J.; Gorski, C. A. Kinetic Drawbacks of Combining Electrochemical CO_2 Sorbent Reactivation with CO_2 Absorption. *Ind. Eng. Chem. Res.* **2023**, *62* (46), 19784–19800. https://doi.org/10.1021/acs.iecr.3c02204.

(39) Wang, M.; Hariharan, S.; Shaw, R. A.; Hatton, T. A. Energetics of Electrochemically Mediated Amine Regeneration Process for Flue Gas CO_2 Capture. *Int. J. Greenh. Gas Control* **2019**, *82*, 48–58. https://doi.org/10.1016/j.ijggc.2018.12.028.

(40) Newman, J.; Balsara, N. P. *Electrochemical Systems*, 4th Edition.; John Wiley & Sons Inc., 2021.

(41) Simeon, F.; Stern, M. C.; Diederichsen, K. M.; Liu, Y.; Herzog, H. J.; Hatton, T. A. Electrochemical and Molecular Assessment of Quinones as CO_2-Binding Redox Molecules for Carbon Capture. *J. Phys. Chem. C* **2022**, *126* (3), 1389–1399. https://doi.org/10.1021/acs.jpcc.1c09415.

(42) Scott, K. Reactor Modelling for Electrochemical Processes. *J. Chem. Technol. Biotechnol.* **1992**, *54* (3), 257–266. https://doi.org/10.1002/jctb.280540308.

(43) Wendt, H.; Kreysa, G. Electrochemical Reaction Engineering. In *Electrochemical Engineering: Science and Technology in Chemical and Other Industries*; Wendt, H., Kreysa, G., Eds.; Springer: Berlin, Heidelberg, 1999; pp 128–152. https://doi.org/10.1007/978-3-662-03851-2_6.

(44) Goodridge, F.; Scott, K. *Electrochemical Process Engineering: A Guide to the Design of Electrolytic Plant*; Springer Science + Business Media, LLC, 1995.

(45) Reimer, U.; Lehnert, W.; Holade, Y.; Kokoh, B. Irreversible Losses in Fuel Cells. In *Fuel Cells and Hydrogen*; Hacker, V., Mitsushima, S., Eds.; Elsevier, 2018; pp 15–40. https://doi.org/10.1016/B978-0-12-811459-9.00002-5.

(46) Conejo, A. N. *Fundamentals of Dimensional Analysis: Theory and Applications in Metallurgy*; Springer Nature Singapor Pte Ltd., 2021.

(47) Zito, A. M.; Clarke, L. E.; Barlow, J. M.; Bím, D.; Zhang, Z.; Ripley, K. M.; Li, C. J.; Kummeth, A.; Leonard, M. E.; Alexandrova, A. N.; Brushett, F. R.; Yang, J. Y. Electrochemical Carbon Dioxide Capture and Concentration. *Chem. Rev.* **2023**, *123* (13), 8069–8098. https://doi.org/10.1021/acs.chemrev.2c00681.

(48) Scovazzo, P.; Poshusta, J.; DuBois, D.; Koval, C.; Noble, R. Electrochemical Separation and Concentration of <1% Carbon Dioxide from Nitrogen. *J. Electrochem. Soc.* **2003**, *150* (5), D91. https://doi.org/10.1149/1.1566962.

(49) Gurkan, B.; Simeon, F.; Hatton, T. A. Quinone Reduction in Ionic Liquids for Electrochemical CO2 Separation. *ACS Sustain. Chem. Eng.* **2015**, *3* (7), 1394–1405. https://doi.org/10.1021/acssuschemeng.5b00116.

(50) Ji, X.; Banks, C. E.; Silvester, D. S.; Wain, A. J.; Compton, R. G. Electrode Kinetic Studies of the Hydroquinone−Benzoquinone System and the Reaction between Hydroquinone and Ammonia in Propylene Carbonate: Application to the Indirect Electroanalytical Sensing of Ammonia. *J. Phys. Chem. C* **2007**, *111* (3), 1496–1504. https://doi.org/10.1021/jp066704y.

(51) König, M.; Vaes, J.; Pant, D.; Klemm, E. Effect of Solvents on Aprotic CO_2 Reduction: A Study on the Role of CO_2 Mass Transport in the Product Selectivity between Oxalate and Carbon Monoxide. *J. Phys. Chem. C* **2023**, *127* (36), 18159–18166. https://doi.org/10.1021/acs.jpcc.3c03992.

(52) Comeau Simpson, T.; Durand, R. R. Reactivity of Carbon Dioxide with Quinones. *Electrochimica Acta* **1990**, *35* (9), 1399–1403. https://doi.org/10.1016/0013-4686(90)85012-C.

(53) Lehmann, M. W.; Evans, D. H. Anomalous Behavior in the Two-Step Reduction of Quinones in Acetonitrile. *J. Electroanal. Chem.* **2001**, *500* (1), 12–20. https://doi.org/10.1016/S0022-0728(00)00234-5.

(54) Barlow, J. M.; Clarke, L. E.; Zhang, Z.; Bím, D.; Ripley, K. M.; Zito, A.; Brushett, F. R.; Alexandrova, A. N.; Yang, J. Y. Molecular Design of Redox Carriers for Electrochemical CO_2 Capture and Concentration. *Chem. Soc. Rev.* **2022**, *51* (20), 8415–8433. https://doi.org/10.1039/D2CS00367H.

(55) Neyhouse, B. J.; Fenton, A. M.; Brushett, F. R. Too Much of a Good Thing? Assessing Performance Tradeoffs of Two-Electron Compounds for Redox Flow Batteries. *J. Electrochem. Soc.* **2021**, *168* (5), 050501. https://doi.org/10.1149/1945-7111/abeea3.

(56) Barlow, J. M.; Yang, J. Y. Oxygen-Stable Electrochemical CO_2 Capture and Concentration with Quinones Using Alcohol Additives. *J. Am. Chem. Soc.* **2022**, *144* (31), 14161–14169. https://doi.org/10.1021/jacs.2c04044.

(57) Li, X.; Zhao, X.; Zhang, L.; Mathur, A.; Xu, Y.; Fang, Z.; Gu, L.; Liu, Y.; Liu, Y. Redox-Tunable Isoindigos for Electrochemically Mediated Carbon Capture. *Nat. Commun.* **2024**, *15* (1), 1175. https://doi.org/10.1038/s41467-024-45410-z.

(58) Oloman, C.; Li, H. Electrochemical Processing of Carbon Dioxide. *ChemSusChem* **2008**, *1* (5), 385–391. https://doi.org/10.1002/cssc.200800015.

(59) Spurgeon, J. M.; Kumar, B. A Comparative Technoeconomic Analysis of Pathways for Commercial Electrochemical CO_2 Reduction to Liquid Products. *Energy Environ. Sci.* **2018**, *11* (6), 1536–1551. https://doi.org/10.1039/C8EE00097B.

(60) Zhang, M.; Moore, M.; Watson, J. S.; Zawodzinski, T. A.; Counce, R. M. Capital Cost Sensitivity Analysis of an All-Vanadium Redox-Flow Battery. *J. Electrochem. Soc.* **2012**, *159* (8), A1183. https://doi.org/10.1149/2.041208jes.

(61) Muroyama, A. P.; Beard, A.; Pribyl-Kranewitter, B.; Gubler, L. Separation of CO_2 from Dilute Gas Streams Using a Membrane Electrochemical Cell. *ACS EST Eng.* **2021**, *1* (5), 905–916. https://doi.org/10.1021/acsestengg.1c00048.

(62) Arenas, L. F.; León, C. P. de; Walsh, F. C. Mass Transport and Active Area of Porous Pt/Ti Electrodes for the Zn-Ce Redox Flow Battery Determined from Limiting Current Measurements. *Electrochimica Acta* **2016**, *221*, 154–166. https://doi.org/10.1016/j.electacta.2016.10.097.

(63) Arenas, L. F.; Ponce de León, C.; Walsh, F. C. Redox Flow Batteries for Energy Storage: Their Promise, Achievements and Challenges. *Curr. Opin. Electrochem.* **2019**, *16*, 117–126. https://doi.org/10.1016/j.coelec.2019.05.007.

(64) Kinoshita, K.; Leach, S. C. Mass-Transfer Study of Carbon Felt, Flow-Through Electrode. *J. Electrochem. Soc.* **1982**, *129* (9), 1993. https://doi.org/10.1149/1.2124338.

(65) Tenny, K. M.; Forner-Cuenca, A.; Chiang, Y.-M.; Brushett, F. R. Comparing Physical and Electrochemical Properties of Different Weave Patterns for Carbon Cloth Electrodes in Redox Flow Batteries. *J. Electrochem. Energy Convers. Storage* **2020**, *17* (4), 041010. https://doi.org/10.1115/1.4046661.

(66) Incropera, F. P.; Dewitt, D. P.; Bergman, T. L.; Lavine, A. S. *Fundamentals of Heat and Mass Transfer*, 6th ed.; John Wiley & Sons, Inc., 2007.

(67) Jakobsen, H. A. *Chemical Reactor Modeling: Multiphase Reactive Flows*, 1st ed.; Springer-Verlag Berlin Heidelberg, 2008.

(68) Barton, J. L.; Milshtein, J. D.; Hinricher, J. J.; Brushett, F. R. Quantifying the Impact of Viscosity on Mass-Transfer Coefficients in Redox Flow Batteries. *J. Power Sources* **2018**, *399*, 133–143. https://doi.org/10.1016/j.jpowsour.2018.07.046.

(69) Xu, Q.; Zhao, T. S. Determination of the Mass-Transport Properties of Vanadium Ions through the Porous Electrodes of Vanadium Redox Flow Batteries. *Phys. Chem. Chem. Phys.* **2013**, *15* (26), 10841–10848. https://doi.org/10.1039/C3CP51944A.

(70) Simon, B. A.; Gayon-Lombardo, A.; Pino-Muñoz, C. A.; Wood, C. E.; Tenny, K. M.; Greco, K. V.; Cooper, S. J.; Forner-Cuenca, A.; Brushett, F. R.; Kucernak, A. R.; Brandon, N. P. Combining Electrochemical and Imaging Analyses to Understand the Effect of Electrode

Microstructure and Electrolyte Properties on Redox Flow Batteries. *Appl. Energy* **2022**, *306*, 117678. https://doi.org/10.1016/j.apenergy.2021.117678.

(71) You, X.; Ye, Q.; Cheng, P. The Dependence of Mass Transfer Coefficient on the Electrolyte Velocity in Carbon Felt Electrodes: Determination and Validation. *J. Electrochem. Soc.* **2017**, *164* (11), E3386. https://doi.org/10.1149/2.0401711jes.

(72) Zeng, C.; Kim, S.; Chen, Y.; Fu, Y.; Bao, J.; Xu, Z.; Wang, W. In Situ Characterization of Kinetics, Mass Transfer, and Active Electrode Surface Area for Vanadium Redox Flow Batteries. *J. Electrochem. Soc.* **2023**, *170* (3), 030507. https://doi.org/10.1149/1945-7111/acbf7f.

(73) Milshtein, J. D.; Tenny, K. M.; Barton, J. L.; Drake, J.; Darling, R. M.; Brushett, F. R. Quantifying Mass Transfer Rates in Redox Flow Batteries. *J. Electrochem. Soc.* **2017**, *164* (11), E3265. https://doi.org/10.1149/2.0201711jes.

(74) Chatenet, M.; Pollet, B. G.; Dekel, D. R.; Dionigi, F.; Deseure, J.; Millet, P.; Braatz, R. D.; Bazant, M. Z.; Eikerling, M.; Staffell, I.; Balcombe, P.; Shao-Horn, Y.; Schäfer, H. Water Electrolysis: From Textbook Knowledge to the Latest Scientific Strategies and Industrial Developments. *Chem. Soc. Rev.* **2022**, *51* (11), 4583–4762. https://doi.org/10.1039/D0CS01079K.

(75) Li, K.; Fan, Q.; Chuai, H.; Liu, H.; Zhang, S.; Ma, X. Revisiting Chlor-Alkali Electrolyzers: From Materials to Devices. *Trans. Tianjin Univ.* **2021**, *27* (3), 202–216. https://doi.org/10.1007/s12209-021-00285-9.

(76) O'Brien, T. F.; Bommaraju, T. V.; Hine, F. *Handbook of Chlor-Alkali Technology. Volume I: Fundamentals*; Springer Science + Business Media, Inc., 2005.

(77) Sequeira, C. a. C.; Santos, D. M. F. Electrochemical Routes for Industrial Synthesis. *J. Braz. Chem. Soc.* **2009**, *20*, 387–406. https://doi.org/10.1590/S0103-50532009000300002.

(78) Rosanske, T. W.; Evans, D. H. Rate Constants for the Electrode Reactions of Some Quinones in Aprotic Media at Platinum, Gold and Mercury Electrodes. *J. Electroanal. Chem. Interfacial Electrochem.* **1976**, *72* (3), 277–285. https://doi.org/10.1016/S0022-0728(76)80314-2.

(79) Hoon, M.; Fawcett, W. R. Kinetics of the Electroreduction and Electrooxidation of Tetrakis(Dimethylamino)-p- Benzoquinone in Polar Aprotic Solvents. *J. Phys. Chem. A* **1997**, *101* (20), 3726–3730. https://doi.org/10.1021/jp963704x.

(80) Nagaoka, T.; Okazaki, S. Electron-Transfer Kinetics of Quinones at Solid Electrodes in Aprotic Solvents at Low Temperatures. *J. Phys. Chem.* **1985**, *89* (11), 2340–2344. https://doi.org/10.1021/j100257a039.

(81) Crooks, R. M.; Bard, A. J. Electrochemistry in Near-Critical and Supercritical Fluids: Part VI. The Electrochemistry of Ferrocene and Phenazine in Acetonitrile between 25 and 300°

C. *J. Electroanal. Chem. Interfacial Electrochem.* **1988**, *243* (1), 117–131. https://doi.org/10.1016/0022-0728(88)85033-2.

(82) Sawyer, D. T.; Komai, R. Y. Electrochemistry of Phenazine at a Platinum Electrode in Aprotic Solvents. *Anal. Chem.* **1972**, *44* (4), 715–721. https://doi.org/10.1021/ac60312a002.

(83) Duan, W.; Huang, J.; Kowalski, J. A.; Shkrob, I. A.; Vijayakumar, M.; Walter, E.; Pan, B.; Yang, Z.; Milshtein, J. D.; Li, B.; Liao, C.; Zhang, Z.; Wang, W.; Liu, J.; Moore, J. S.; Brushett, F. R.; Zhang, L.; Wei, X. "Wine-Dark Sea" in an Organic Flow Battery: Storing Negative Charge in 2,1,3-Benzothiadiazole Radicals Leads to Improved Cyclability. *ACS Energy Lett.* **2017**, *2* (5), 1156–1161. https://doi.org/10.1021/acsenergylett.7b00261.

(84) Eigeldinger, J.; Vogt, H. The Bubble Coverage of Gas-Evolving Electrodes in a Flowing Electrolyte. *Electrochimica Acta* **2000**, *45* (27), 4449–4456. https://doi.org/10.1016/S0013-4686(00)00513-2.

(85) Ateya, B. G.; El-Anadouli, B. E. Effects of Gas Bubbles on the Polarization Behavior of Porous Flow Through Electrodes. *J. Electrochem. Soc.* **1991**, *138* (5), 1331. https://doi.org/10.1149/1.2085781.

(86) Darling, R. M.; Gallagher, K. G.; Kowalski, J. A.; Ha, S.; Brushett, F. R. Pathways to Low-Cost Electrochemical Energy Storage: A Comparison of Aqueous and Nonaqueous Flow Batteries. *Energy Env. Sci* **2014**, *7* (11), 3459–3477. https://doi.org/10.1039/C4EE02158D.

(87) Milshtein, J. D.; Barton, J. L.; Carney, T. J.; Kowalski, J. A.; Darling, R. M.; Brushett, F. R. Towards Low Resistance Nonaqueous Redox Flow Batteries. *J. Electrochem. Soc.* **2017**, *164* (12), A2487. https://doi.org/10.1149/2.0741712jes.

(88) Hudak, N. S.; Small, L. J.; Pratt, H. D.; Anderson, T. M. Through-Plane Conductivities of Membranes for Nonaqueous Redox Flow Batteries. *J. Electrochem. Soc.* **2015**, *162* (10), A2188. https://doi.org/10.1149/2.0901510jes.

(89) Kim, J.; Park, H. Experimental Analysis of Discharge Characteristics in Vanadium Redox Flow Battery. *Appl. Energy* **2017**, *206*, 451–457. https://doi.org/10.1016/j.apenergy.2017.08.218.

(90) Liu, Q. H.; Grim, G. M.; Papandrew, A. B.; Turhan, A.; Zawodzinski, T. A.; Mench, M. M. High Performance Vanadium Redox Flow Batteries with Optimized Electrode Configuration and Membrane Selection. *J. Electrochem. Soc.* **2012**, *159* (8), A1246. https://doi.org/10.1149/2.051208jes.

(91) Gerhardt, M. R.; Pant, L. M.; Bui, J. C.; Crothers, A. R.; Ehlinger, V. M.; Fornaciari, J. C.; Liu, J.; Weber, A. Z. Method—Practices and Pitfalls in Voltage Breakdown Analysis of Electrochemical Energy-Conversion Systems. *J. Electrochem. Soc.* **2021**, *168* (7), 074503. https://doi.org/10.1149/1945-7111/abf061.

TOC Graphic